

1 SEARCH FOR PRODUCTION OF A HIGGS BOSON AND A SINGLE TOP  
2 QUARK IN MULTILEPTON FINAL STATES IN  $pp$  COLLISIONS AT  $\sqrt{s} = 13$   
3 TeV.

4 by

5 Jose Andres Monroy Montañez

# A DISSERTATION

7 Presented to the Faculty of

8 The Graduate College at the University of Nebraska

In Partial Fulfilment of Requirements

10 For the Degree of Doctor of Philosophy

11 Major: Physics and Astronomy

12 Under the Supervision of Kenneth Bloom and Aaron Dominguez

13 Lincoln, Nebraska

14 July, 2018

15 SEARCH FOR PRODUCTION OF A HIGGS BOSON AND A SINGLE TOP  
16 QUARK IN MULTILEPTON FINAL STATES IN pp COLLISIONS AT  $\sqrt{s} = 13$   
17 TeV.

18 Jose Andres Monroy Montañez, Ph.D.

19 University of Nebraska, 2018

20 Adviser: Kenneth Bloom and Aaron Dominguez

# **21 Table of Contents**

<b>22 Table of Contents</b>	<b>iii</b>
<b>23 List of Figures</b>	<b>v</b>
<b>24 List of Tables</b>	<b>vii</b>
<b>25 3 The CMS experiment at the LHC</b>	<b>1</b>
26     3.1 Introduction . . . . .	1
27     3.2 The LHC . . . . .	2
28     3.3 The CMS experiment . . . . .	12
29         3.3.1 Coordinate system . . . . .	14
30         3.3.2 Pixels detector . . . . .	15
31         3.3.3 Silicon strip tracker . . . . .	17
32         3.3.4 Electromagnetic calorimeter . . . . .	19
33         3.3.5 Hadronic calorimeter . . . . .	20
34         3.3.6 Superconducting solenoid magnet . . . . .	22
35         3.3.7 Muon system . . . . .	23
36         3.3.8 CMS trigger system . . . . .	24
37         3.3.9 CMS computing . . . . .	26

38	<b>4 Event generation, simulation and reconstruction</b>	<b>30</b>
39	4.1 Event generation . . . . .	31
40	4.2 Monte Carlo Event Generators. . . . .	35
41	4.3 CMS detector simulation. . . . .	36
42	4.4 Event reconstruction. . . . .	38
43	4.4.1 Particle-Flow Algorithm. . . . .	38
44	4.4.1.1 Missing transverse energy. . . . .	50
45	4.4.2 Event reconstruction examples . . . . .	51
46	<b>Bibliography</b>	<b>51</b>
47	<b>References</b>	<b>54</b>

## <sup>48</sup> List of Figures

49	3.1 CERN accelerator complex . . . . .	2
50	3.2 LHC protons source. First acceleration stage. . . . .	3
51	3.3 The LINAC2 accelerating system at CERN. . . . .	4
52	3.4 LHC layout and RF cavities module. . . . .	5
53	3.5 LHC dipole magnet. . . . .	7
54	3.6 Integrated luminosity delivered by LHC and recorded by CMS during 2016	9
55	3.7 LHC interaction points . . . . .	10
56	3.8 Multiple $pp$ collision bunch crossing at CMS. . . . .	12
57	3.9 Layout of the CMS detector . . . . .	13
58	3.10 CMS detector coordinate system . . . . .	14
59	3.11 CMS pixel detector schematic view. . . . .	17
60	3.12 SST Schematic view. . . . .	18
61	3.13 CMS ECAL schematic view . . . . .	19
62	3.14 CMS HCAL schematic view . . . . .	21
63	3.15 CMS solenoid magnet . . . . .	22
64	3.16 CMS Muon system schematic view . . . . .	23
65	3.17 CMS Level-1 trigger architecture . . . . .	25
66	3.18 WLCG structure . . . . .	27

67	3.19 Data flow from CMS detector through hardware Tiers . . . . .	29
68	4.1 Event generation process. . . . .	31
69	4.2 Particle flow algorithm. . . . .	39
70	4.3 Jet reconstruction. . . . .	47
71	4.4 Jet energy corrections. . . . .	48
72	4.5 Secondary vertex in a b-hadron decay. . . . .	49
73	4.6 HIG-13-004 Event 1 reconstruction. . . . .	51
74	4.7 $e\mu$ event reconstruction. . . . .	52
75	4.8 Recorded event reconstruction. . . . .	53

<sup>76</sup> **List of Tables**

## <sup>77</sup> Chapter 3

### <sup>78</sup> The CMS experiment at the LHC

#### <sup>79</sup> 3.1 Introduction

<sup>80</sup> Located on the Swiss-French border, the European Council for Nuclear Research  
<sup>81</sup> (CERN) is the largest scientific organization leading the particle physics research.  
<sup>82</sup> About 13000 people in a broad range of fields including users, students, scientists,  
<sup>83</sup> engineers, among others, contribute to the data taking and analysis, with the goal  
<sup>84</sup> of unveiling the secrets of nature and revealing the fundamental structure of the  
<sup>85</sup> universe. CERN is also the home of the Large Hadron Collider (LHC), the largest  
<sup>86</sup> circular particle accelerator around the world, where protons (or heavy ions) traveling  
<sup>87</sup> close to the speed of light, are made to collide. These collisions open a window  
<sup>88</sup> to investigate how particles (and their constituents if they are composite) interact  
<sup>89</sup> with each other, providing clues about the laws of nature. This chapter presents an  
<sup>90</sup> overview of the LHC structure and operation. A detailed description of the CMS  
<sup>91</sup> detector is offered, given that the data used in this thesis have been taken with this  
<sup>92</sup> detector.

### 93 3.2 The LHC

94 With 27 km of circumference, the LHC is currently the largest and most powerful  
 95 circular accelerator in the world. It is installed in the same tunnel where the Large  
 96 Electron-Positron (LEP) collider was located, taking advantage of the existing infras-  
 97 tructure. The LHC is also the larger accelerator in the CERN's accelerator complex  
 98 and is assisted by several successive accelerating stages before the particles are in-  
 99 jected into the LHC ring where they reach their maximum energy (see Figure 3.1).

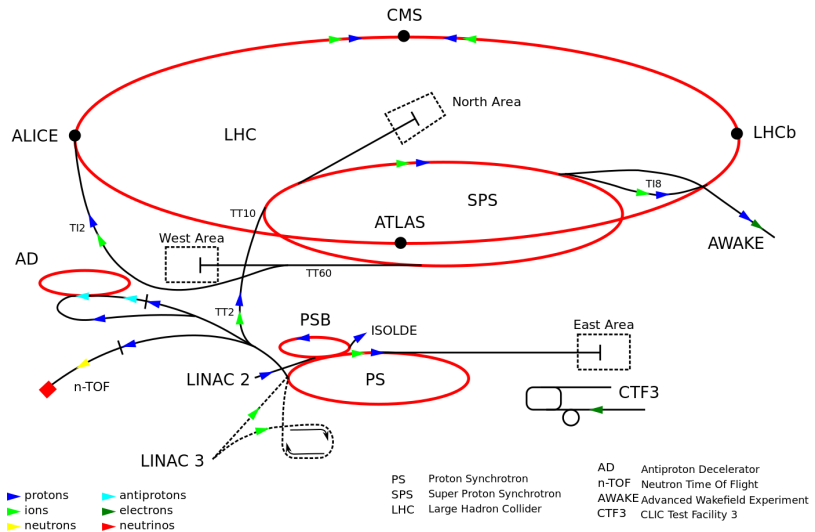


**Figure 3.1:** CERN accelerator complex. Blue arrows show the path followed by protons along the acceleration process [54].

100 LHC runs in three modes depending on the particles being accelerated

- 101     • Proton-Proton collisions ( $pp$ ) for multiple physics experiments.
- 102     • Lead-Lead collisions ( $Pb-Pb$ ) for heavy ion experiments.
- 103     • Proton-Lead collisions ( $p-Pb$ ) for quark-gluon plasma experiments.

104 In this thesis only  $pp$  collisions will be considered.

105

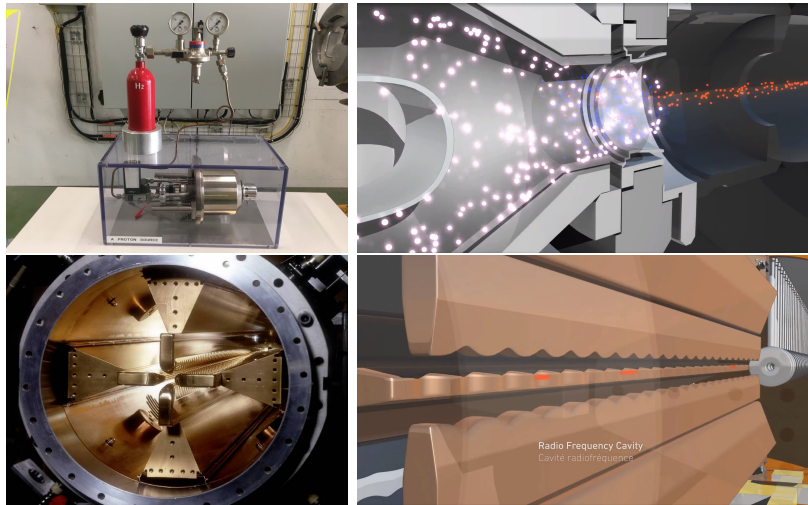


**Figure 3.2:** LHC protons source and the first acceleration stage. Top: the bottle contains hydrogen gas (white dots) which is injected into the metal cylinder to be broken down into electrons (blue dots) and protons (red dots); Bottom: the obtained protons are directed towards the radio frequency quadrupole which perform the first acceleration, focus the beam and create the bunches of protons. [58, 59]

106 Collection of protons starts with hydrogen atoms taken from a bottle, containing hy-  
 107 drogen gas, and injecting them in a metal cylinder; hydrogen atoms are broken down  
 108 into electrons and protons by an intense electric field (see Figure 3.2 top). The re-  
 109 sulting protons leave the metal cylinder towards a radio frequency quadrupole (RFQ)  
 110 that focus the beam, accelerates the protons and creates the packets of protons called  
 111 bunches. In the RFQ, an electric field is generated by a RF wave at a frequency that  
 112 matches the resonance frequency of the cavity where the electrodes are contained.  
 113 The beam of protons traveling on the RFQ axis experiences an alternating electric  
 114 field gradient that generates the focusing forces.

115

116 In order to accelerate the protons, a longitudinal time-varying electric field component  
 117 is added to the system; it is done by giving the electrodes a sinus-like profile as shown  
 118 in Figure 3.2 bottom. By matching the speed and phase of the protons with the  
 119 longitudinal electric field the bunching is performed; protons synchronized with the

120 RFQ (synchronous proton) do not feel an accelerating force, but those protons in the  
 121 beam that have more (or less) energy than the synchronous proton (asynchronous  
 122 protons) will feel a decelerating (accelerating) force; therefore, asynchronous protons  
 123 will oscillate around the synchronous ones forming bunches of protons [56]. From the  
 124 RFQ protons emerge with energy 750 keV in bunches of about  $1.15 \times 10^{11}$  protons [57].

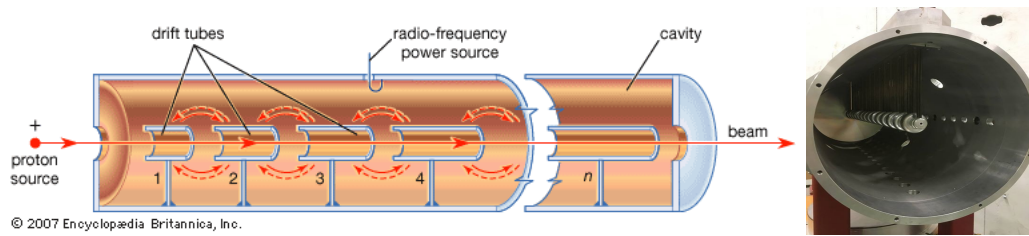


**Figure 3.3:** The LINAC2 accelerating system at CERN. Electric fields generated by radio frequency (RF) create acceleration and deceleration zones inside the cavity; deceleration zones are blocked by drift tubes where quadrupole magnets focus the proton beam. [60]

125 Proton bunches coming from the RFQ go to the linear accelerator 2 (LINAC2) where  
 126 they are accelerated to reach 50 MeV energy. In the LINAC2 stage, acceleration  
 127 is performed using electric fields generated by radio frequency which create zones  
 128 of acceleration and deceleration as shown in Figure 3.3. In the deceleration zones,  
 129 the electric field is blocked using drift tubes where protons are free to drift while  
 130 quadrupole magnets focus the beam.

131

132 The beam coming from LINAC2 is injected into the proton synchrotron booster  
 133 (PSB) to reach 1.4 GeV in energy. The next acceleration is provided at the pro-  
 134 ton synchrotron (PS) up to 26 GeV, followed by the injection into the super proton  
 135 synchrotron (SPS) where protons are accelerated to 450 GeV. Finally, protons are  
 136 injected into the LHC where they are accelerated to the target energy of 6.5 TeV.  
 137 PSB, PS, SPS and LHC accelerate protons using the same RF acceleration technique  
 138 described before.

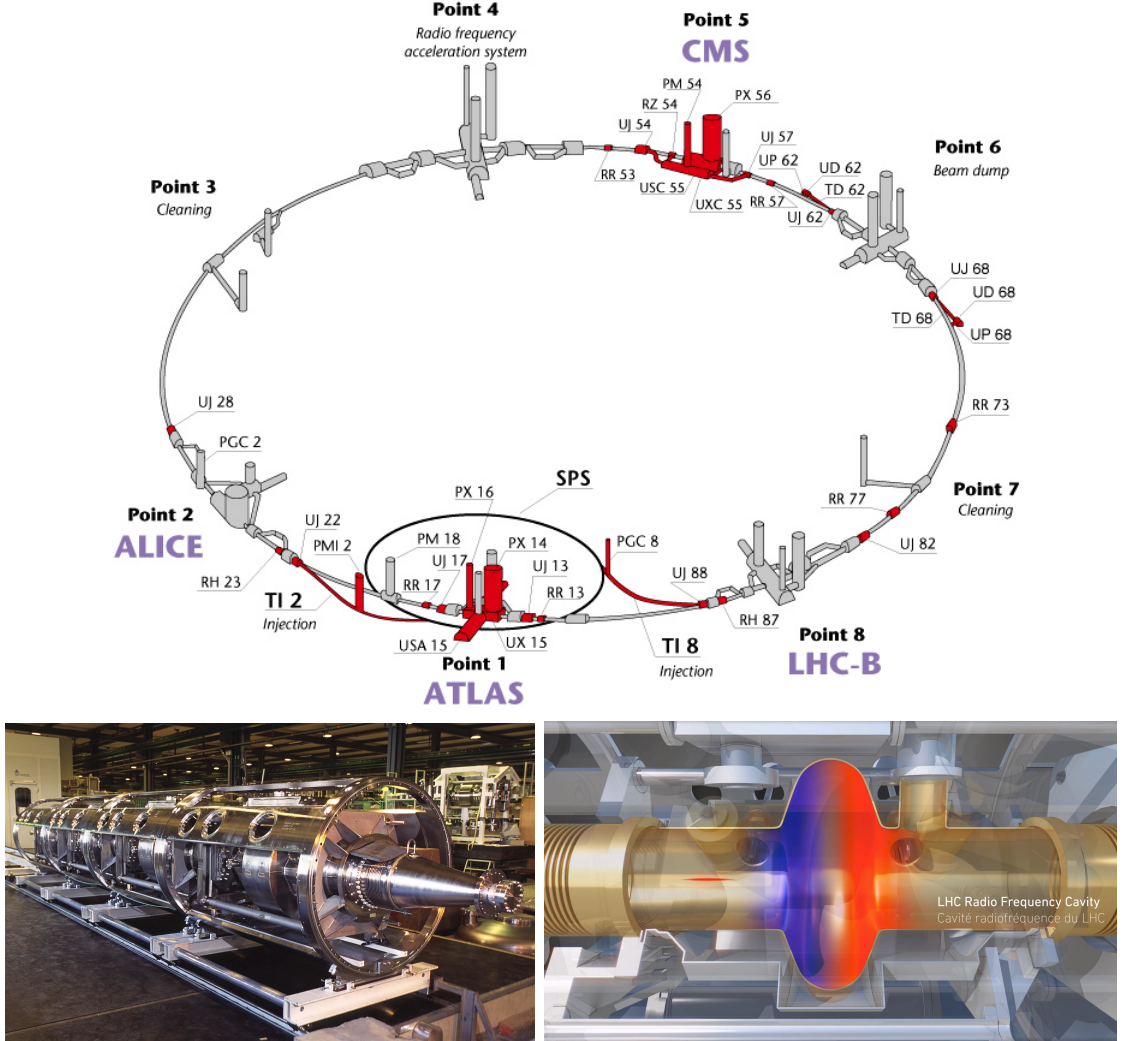


**Figure 3.4:** Top: LHC layout. The red zones indicate the infrastructure additions to the LEP installations, built to accommodate the ATLAS and CMS experiments which exceed the size of the former experiments located there [55]. Bottom: LHC RF cavities. A module accommodates 4 cavities that accelerate protons and preserve the bunch structure of the beam. [59, 61]

139 LHC has a system of 16 RF cavities located in the so-called point 4, as shown in  
 140 Figure 3.4 top, tuned at a frequency of 400 MHz and the protons are carefully timed,  
 141 so in addition to the acceleration effect the bunch structure of the beam is preserved.  
 142 Bottom side of Figure 3.4 shows a picture of a RF module composed of 4 RF cavities  
 143 working in a superconducting state at 4.5 K; also is showed a representation of the

144 accelerating electric field that accelerates the protons in the bunch.

145

146 While protons are accelerated in one section of the LHC ring, where the RF cavities  
 147 are located, in the rest of their path they have to be kept in the curved trajectory  
 148 defined by the LHC ring. Technically, LHC is not a perfect circle; RF, injection, beam  
 149 dumping, beam cleaning and sections before and after the experimental points where  
 150 protons collide are all straight sections. In total, there are 8 arcs 2.45 Km long each  
 151 and 8 straight sections 545 m long each. In order to curve the proton's trajectory in  
 152 the arc sections, superconducting dipole magnets are used.

153

154 Inside the LHC ring, there are two proton beams traveling in opposite directions in  
 155 two separated beam pipes; the beam pipes are kept at ultra-high vacuum ( $\sim 10^{-9}$   
 156 Pa) to ensure that there are no particles that interact with the proton beams. The  
 157 superconducting dipole magnets used in LHC are made of a NbTi alloy, capable of  
 158 transporting currents of about 12000 A when cooled at a temperature below 2K using  
 159 liquid helium (see Figure 3.5).

160

161 Protons in the arc sections of LHC feel a centripetal force exerted by the dipole  
 162 magnets which is perpendicular to the beam trajectory; The magnitude of magnetic  
 163 field needed can be found assuming that protons travel at  $v \approx c$ , using the standard  
 164 values for proton mass and charge and the LHC radius, as

$$F_m = \frac{mv^2}{r} = qBv \quad \rightarrow B = 8.33T \quad (3.1)$$

165 which is about 100000 times the Earth's magnetic field. A representation of the mag-  
 166 netic field generated by the dipole magnets is shown on the bottom left side of Figure

### LHC DIPOLE : STANDARD CROSS-SECTION

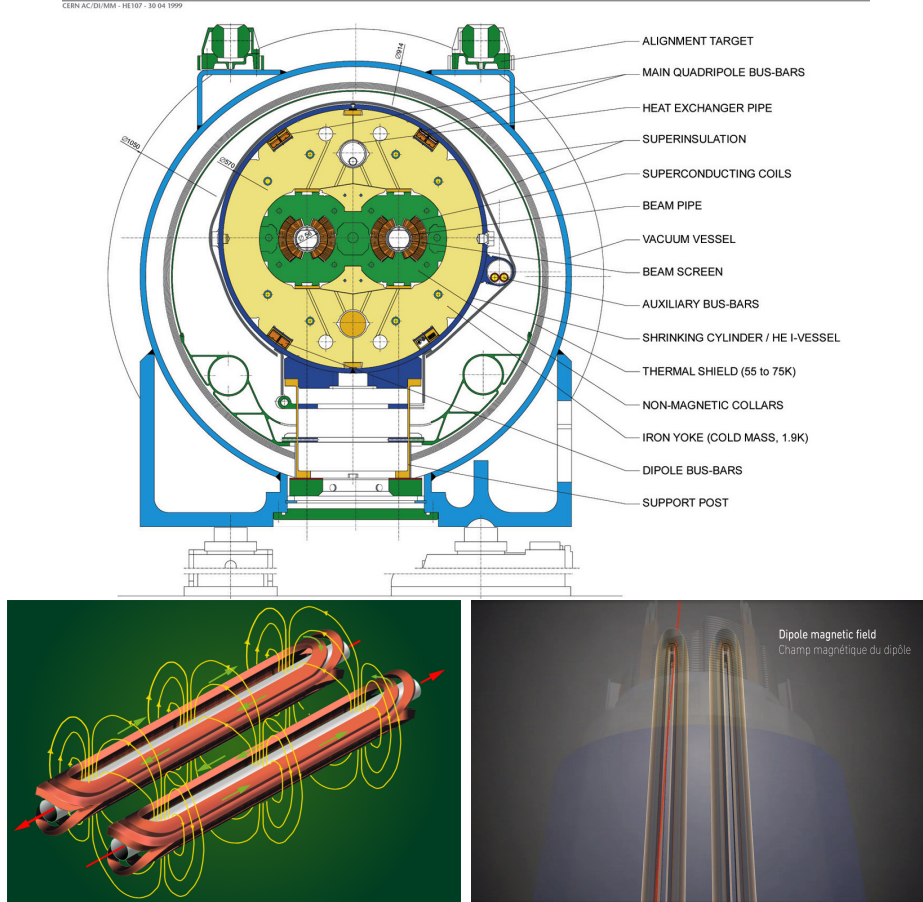


**Figure 3.5:** Top: LHC dipole magnet transverse view; cooling, shielding and mechanical support are indicated. Bottom left: Magnetic field generated by the dipole magnets; note that the direction of the field inside one beam pipe is opposite with respect to the other beam pipe which guarantee that both proton beams are curved in the same direction towards the center of the ring. The effect of the dipole magnetic field on the proton beam is represented on the bottom right side [59, 62, 63].

167 3.5. The bending effect of the magnetic field on the proton beam is shown on the  
 168 bottom right side of Figure 3.5. Note that the dipole magnets are not curved; the  
 169 arc section of the LHC ring is composed of straight dipole magnets of about 15 m.  
 170 In total there are 1232 dipole magnets along the LHC ring.

171

172 In addition to bending the beam trajectory, the beam has to be focused so it stays

173 inside the beam pipe. The focusing is performed by quadrupole magnets installed in  
 174 a different straight section; in total 858 quadrupole magnets are installed along the  
 175 LHC ring. Other effects like electromagnetic interaction among bunches, interaction  
 176 with electron clouds from the beam pipe, the gravitational force on the protons, dif-  
 177 ferences in energy among protons in the same bunch, among others, are corrected  
 178 using sextupole and other magnetic multipoles.

179

180 The two proton beams inside the LHC ring are made of bunches with a cylindrical  
 181 shape of about 7.5 cm long and about 1 mm in diameter; when bunches are close  
 182 to the collision point (CP), the beam is focused up to a diameter of about 16  $\mu\text{m}$  in  
 183 order to maximize the number of collisions per unit area and per second, known as  
 184 luminosity ( $L$ ). Luminosity can be calculated using

$$L = fn \frac{N_1 N_2}{4\pi\sigma_x\sigma_y} \quad (3.2)$$

185 where  $f$  is the revolution frequency,  $n$  is the number of bunches per beam,  $N_1$  and  
 186  $N_2$  are the numbers of protons per bunch ( $1.5 \times 10^{11}$ ),  $\sigma_x$  and  $\sigma_y$  are the gaussian  
 187 transverse sizes of the bunches. The expected luminosity is about

$$f = \frac{v}{2\pi r_{LHC}} \approx \frac{3 \times 10^8 \text{ m/s}}{27 \text{ km}} \approx 11.1 \text{ kHz},$$

$$n = 2808$$

$$N_1 = N_2 = 1.5 \times 10^{11}$$

$$\sigma_x = \sigma_y = 16 \mu\text{m}$$

188

$$L = 1.28 \times 10^{34} \text{ cm}^{-2} \text{ s}^{-1} = 1.28 \times 10^{-5} \text{ fb}^{-1} \text{ s}^{-1} \quad (3.3)$$

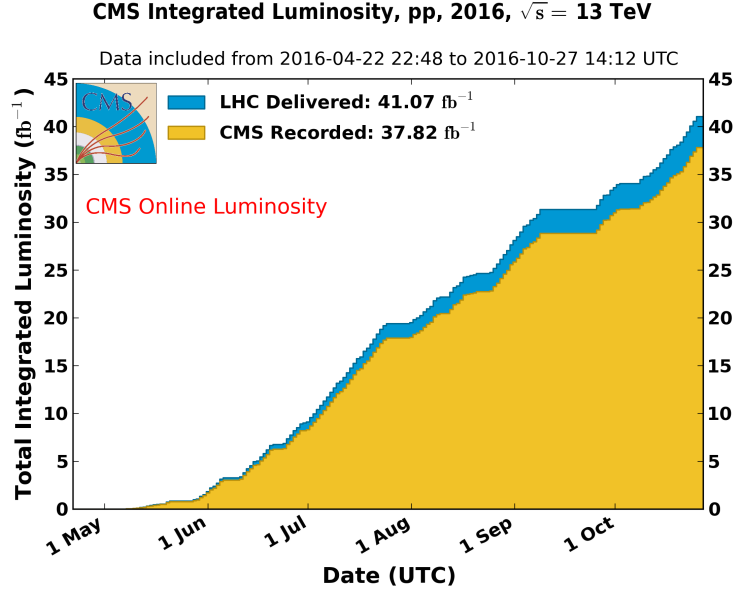


**Figure 3.6:** Integrated luminosity delivered by LHC and recorded by CMS during 2016. The difference between the delivered and the recorded luminosity is due to fails and issues occurred during the data taking in the CMS experiment [64].

189 Luminosity is a fundamental aspect of LHC given that the bigger luminosity the  
 190 bigger number of collisions, which means that for processes with a very small cross  
 191 section the number of expected occurrences is increased and so the chances of being  
 192 detected. The integrated luminosity, i.e., the total luminosity, collected by the CMS  
 193 experiment during 2016 is shown in Figure 3.6; the data analyzed in this thesis cor-  
 194 responds to an integrated luminosity of  $35.9 \text{ fb}^{-1}$  at a center of mass-energy  $\sqrt{s} = 13$   
 195 TeV.

196

197 A way to increase  $L$  is increasing the number of bunches in the beam. Currently, the  
 198 separation between two consecutive bunches in the beam is 7.5 m which corresponds  
 199 to a time separation of 25 ns. In the full LHC ring the allowed number of bunches is  
 200  $n = 27\text{km}/7.5\text{m} = 3600$ ; however, there are some gaps in the bunch pattern intended  
 201 for preparing the dumping and injection of the beam, thus, the proton beams are

202 composed of 2808 bunches.

203

204 Once the proton beams reach the desired energy, they are brought to cross each other  
 205 producing proton-proton collisions. The bunch crossing happens in precise places  
 206 where the four LHC experiments are located, as seen in the top of Figure 3.7. In  
 207 2008, the first set of collisions involved protons with  $\sqrt{s} = 7$  TeV; the energy was  
 208 increased to 8 TeV in 2012 and to 13 TeV in 2015.

209

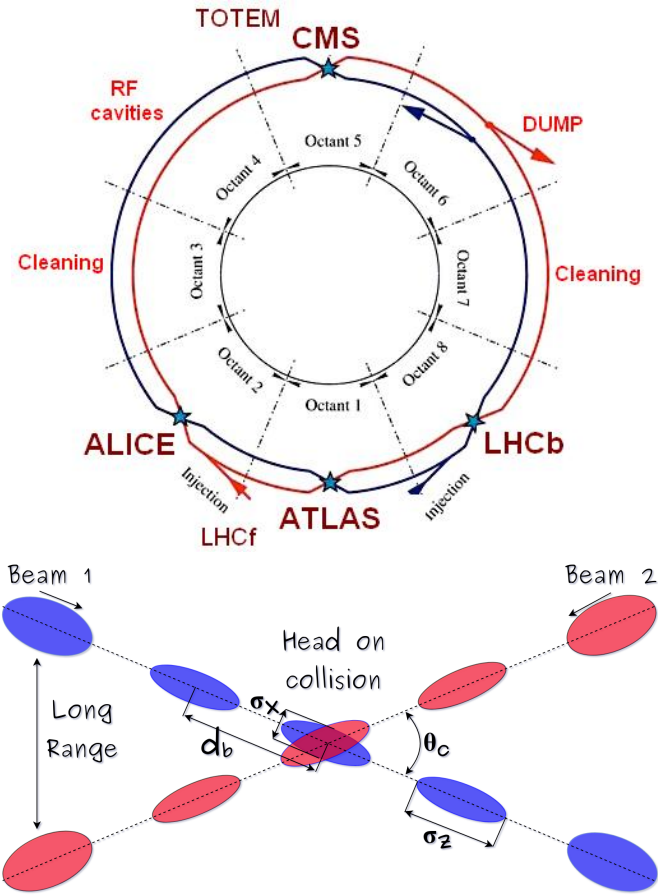


**Figure 3.7:** Top: LHC interaction points. Bunch crossing occurs where the LHC experiments are located [65]. Sections indicated as cleaning are dedicated to collimate the beam in order to protect the LHC ring from collisions with protons in very spreaded bunches. Bottom: bunch crossing scheme. Since the bunch crossing is not perfectly head-on, the luminosity is reduced in a factor of 17%; adapted from Reference [77].

210 CMS and ATLAS experiments, which are multi-purpose experiments, are enabled  
 211 to explore physics in any of the collision modes. LHCb experiment is optimized  
 212 to explore bottom quark physics, while ALICE is optimized for heavy ion collisions  
 213 searches; TOTEM and LHCf are dedicated to forward physics studies; MoEDAL (not  
 214 indicated in the Figure) is intended for monopoles or massive pseudo stable particles  
 215 searches.

216

217 At the CP there are two interesting details that need to be addressed. The first one  
 218 is that the bunch crossing does not occur head-on but at a small crossing angle  $\theta_c$   
 219 (280  $\mu$ rad in CMS and ATLAS) as shown in the bottom side of Figure 3.7, affecting  
 220 the overlapping between bunches; the consequence is a reduction of about 17% in  
 221 the luminosity (represented by a factor not included in eqn. 3.2). The second one  
 222 is the occurrence of multiple  $pp$  collisions in the same bunch crossing; this effect is  
 223 called pile-up (PU). A fairly simple estimation of the PU follows from estimating the  
 224 probability of collision between two protons, one from each of the bunches in course  
 225 of collision; it depends roughly on the ratio of proton size and the cross section of the  
 226 bunch in the interaction point, i.e.,

$$P(pp\text{-}collision) \sim \frac{d_{proton}^2}{\sigma_x \sigma_y} = \frac{(1\text{fm})^2}{(16\mu\text{m})^2} \sim 4 \times 10^{-21} \quad (3.4)$$

227 however, there are  $N = 1.15 \times 10^{11}$  protons in a bunch, thus the estimated number of  
 228 collisions in a bunch crossing is

$$PU = N^2 * P(pp\text{-}collision) \sim 50 \text{ } pp\text{-}collision \text{ per bunch crossing}, \quad (3.5)$$

229 about 20 of those  $pp$  collisions are inelastic. Each collision generates a vertex, but  
 230 only the most energetic is considered as a primary vertex; the rest are considered

231 as PU vertices. A multiple  $pp$  collision event in a bunch crossing at CMS is showed  
 232 in Figure 3.8. Unstable particles outgoing from the primary vertex will eventually  
 233 decay; this decay vertex is known as a secondary vertex.

234

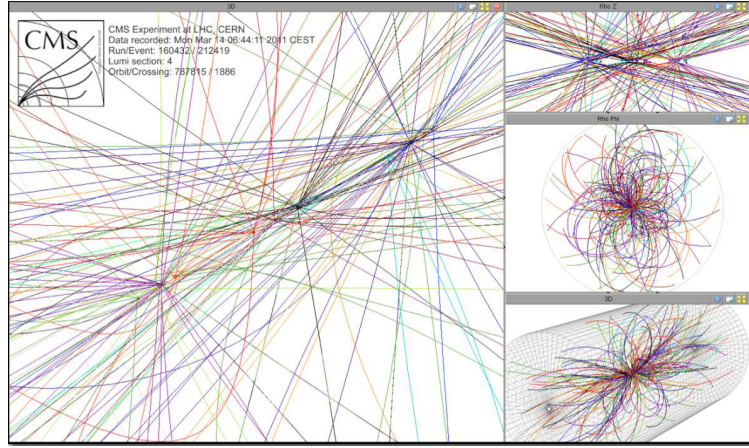


**Figure 3.8:** Multiple  $pp$  collision bunch crossing at CMS. Only the most energetic vertex is considered and the rest are cataloged as PU vertices [66].

235 Next section presents a description of the CMS detector which it is the detector used  
 236 to collect the data used in this thesis.

### 237 3.3 The CMS experiment

238 CMS is a general-purpose detector designed to conduct research in a wide range  
 239 of physics from the standard model to new physics like extra dimensions and dark  
 240 matter. Located at the point 5 in the LHC layout as shown in Figure 3.4, CMS is  
 241 composed of several detection systems distributed in a cylindrical structure; in total,  
 242 CMS weights about 12500 tons in a very compact 21.6 m long and 14.6 m diameter  
 243 cylinder. It was built in 15 separate sections at the ground level and lowered to the  
 244 cavern individually to be assembled. A complete and detailed description of the CMS  
 245 detector and its components is given in Reference [67] on which this section is based

246 on.

247

248 Figure 3.9 shows the layout of the CMS detector. The design is driven by the require-  
 249 ments on the identification, momentum resolution and unambiguous charge determi-  
 250 nation of the muons; therefore, a large bending power is provided by the solenoid  
 251 magnet made of superconducting cable capable to generate a 3.8 T magnetic field.  
 252 The detection system is composed of (from the innermost to the outermost)

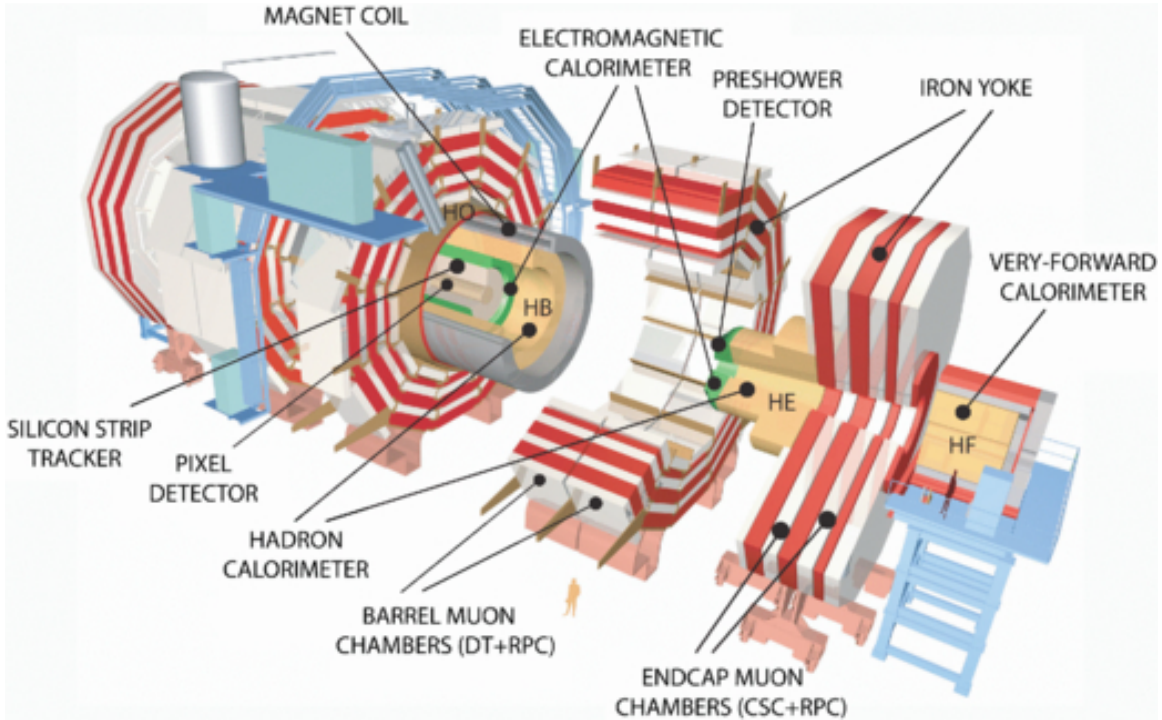


**Figure 3.9:** Layout of the CMS detector. The several subdetectors are indicated. The central region of the detector is referred as the Barrel section while the endcaps are referred as the forward sections. [68].

253 • Pixel detector.

254 • Silicon strip tracker.

255 • Preshower detector.

- 256     • Electromagnetic calorimeter.
- 257     • Hadronic calorimeter.
- 258     • Muon chambers (Barrel and endcap)

259   The central region of the detector is commonly referred as the barrel section while the  
 260   endcaps are referred as the forward sections of the detector; thus, each subdetector  
 261   is composed of a barrel section and a forward section.

### 262   **3.3.1 Coordinate system**

263   The coordinate system used by CMS is centered in the geometrical center of the  
 264   detector which is the same as the CP as shown in Figure 3.10. The  $z$ -axis is parallel  
 265   to the beam direction, while the  $Y$ -axis pointing vertically upward, and the  $X$ -axis  
 266   pointing radially inward toward the center of the LHC.

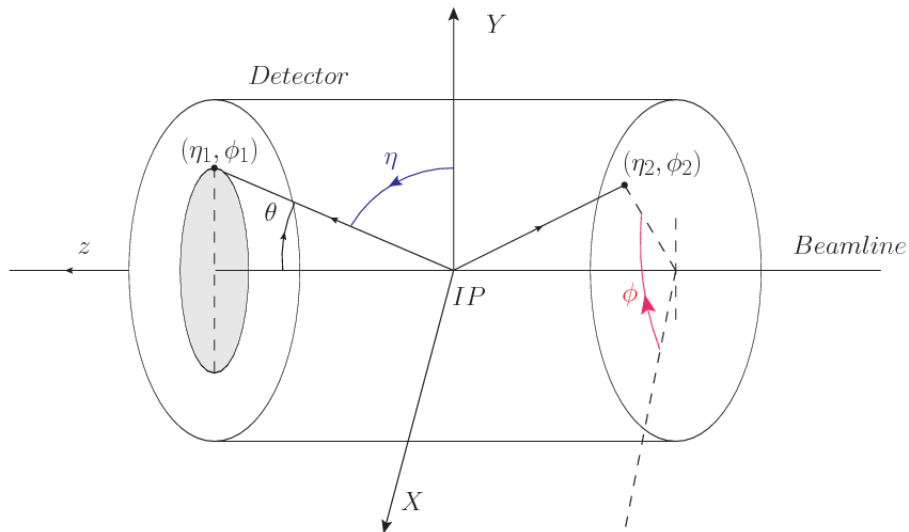


**Figure 3.10:** CMS detector coordinate system.

267   In addition to the common cartesian and cylindrical coordinate systems, two coor-  
 268   dinates are of particular utility in particle physics: rapidity ( $y$ ) and pseudorapidity

269  $(\eta)$ , defined in connection to the polar angle  $\theta$ , energy and longitudinal momentum  
 270 component (momentum along the  $z$ -axis) according to

$$y = \frac{1}{2} \ln \frac{E + p_z}{E - p_z} \quad \eta = -\ln \left( \tan \frac{\theta}{2} \right) \quad (3.6)$$

271 Rapidity is related to the angle between the  $XY$ -plane and the direction in which the  
 272 products of a collision are emitted; it has the nice property that the difference between  
 273 the rapidities of two particles is invariant with respect to Lorentz boosts along the  $z$ -  
 274 axis. Thus, data analysis becomes more simple when based on rapidity; however, it is  
 275 not simple to measure the rapidity of highly relativistic particles, as those produced  
 276 after  $pp$  collisions. Under the highly relativistic motion approximation,  $y$  can be  
 277 rewritten in terms of the polar angle, concluding that rapidity is approximately equal  
 278 to the pseudorapidity defined above, i.e.,  $y \approx \eta$ . Note that  $\eta$  is easier to measure than  $y$   
 279 given the direct relationship between the former and the polar angle. Angular distance  
 280 between two objects in the detector ( $\Delta R$ ) is defined in terms of their coordinates  
 281  $(\eta_1, \phi_1), (\eta_2, \phi_2)$  as

$$\Delta R = \sqrt{(\Delta\eta)^2 - (\Delta\phi)^2} \quad (3.7)$$

### 282 3.3.2 Pixels detector

283 The CMS tracking system is designed to provide a precise measurement of the tra-  
 284 jectory (*track*) followed by the charged particles created after the  $pp$  collisions; also,  
 285 the precise reconstruction of the primary and secondary origins (*vertices*) is expected  
 286 in an environment where, each 25 ns, the bunch crossing produce about 20 inelastic  
 287 collisions and about 1000 particles. An increment in the luminosity is ongoing which  
 288 implies that the PU will increase accordingly.

290 The pixel detector was replaced during the 2016-2017 extended year-end technical  
291 stop, due to the increasingly challenging operating conditions like the higher particle  
292 flow and more radiation harsh environment, among others. The new one is responding  
293 as expected, reinforcing its crucial role in the successful way to fulfill the new LHC  
294 physics objectives after the discovery of the Higgs boson. The last chapter of this  
295 thesis is dedicated to describe my contribution to the *Forward Pixel Phase 1 upgrade*.

296

297 The current pixel detector is composed of 1856 silicon pixel detector modules orga-  
298 nized in four-barrel layers in the central region and three disks in the forward region;  
299 it is designed to record efficiently and with high precision, up to  $10\mu\text{m}$  in the  $XY$ -  
300 plane and  $20\mu\text{m}$  in the  $z$ -direction, the first four space-points (*hits*) near to the CP  
301 region (see Figure 3.11 left side) in the range  $|\eta| \leq 2.5$ . The first barrel layer is located  
302 at a radius of 30 mm from the beamline, while the fourth layer is located at a radius  
303 of 160 mm closer to the strip tracker inner barrel layer (see Section 3.3.3) in order to  
304 reduce the rate of fake tracks. The high granularity of the detector is represented in  
305 its about 123 Mpixels, each of size  $100 \times 150\mu\text{m}^2$ , which is almost twice the channels  
306 of the old detector. The transverse momentum resolution of tracks can be measured  
307 with a resolution of 1-2% for muons of  $p_T = 100$  GeV.

308

309 Some of the improvements with respect to the previous pixel detector include a higher  
310 average tracking efficiency and lower average fake rate as well as higher track impact  
311 parameter resolution which is fundamental in order to increase the efficiency in the  
312 identification of jets originating from b quarks (b-tagging). A significant source of  
313 improvement comes from the overall reduction in the material budget of the detector  
314 which results in fewer photon conversions and less multiple scattering from charged  
315 particles.

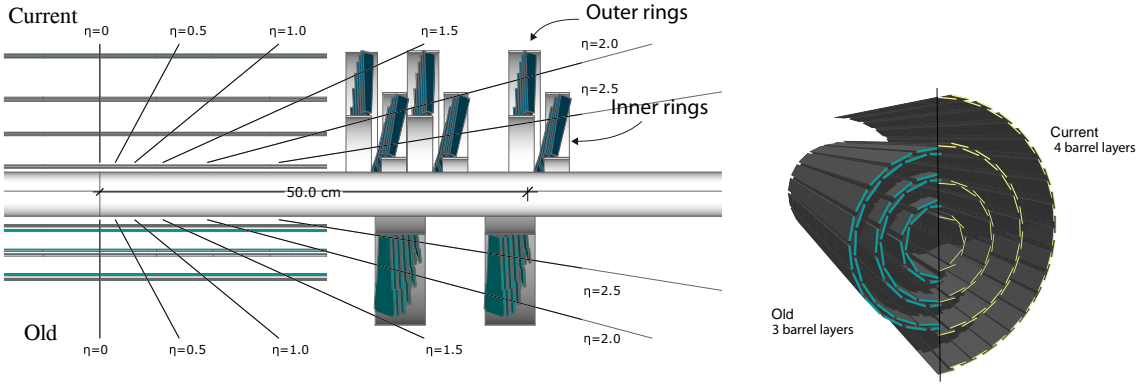


**Figure 3.11:** CMS pixel detector schematic view. Left: layout comparing the layers and disks in the old and current pixel detectors. Right: Transverse-oblique view comparing the pixel barrel layers in the two [70].

### 316 3.3.3 Silicon strip tracker

317 The silicon strip tracker (SST) is the second stage in the CMS tracking system. The  
 318 top side of Figure 3.12 shows a schematic of the SST. The inner tracker region is com-  
 319 posed of the tracker inner barrel (TIB) and the tracker inner disks (TID) covering the  
 320 region  $r < 55$  cm and  $|z| < 118$  cm. The TIB is composed of 4 layers while the TID  
 321 is composed of 3 disks at each end. The silicon sensors in the inner tracker are 320  
 322  $\mu\text{m}$  thick, providing a resolution of about 13-38  $\mu\text{m}$  in the  $r\phi$  position measurement.  
 323

324 The modules indicated in blue in the schematic view of Figure 3.12 are two modules  
 325 mounted back-to-back and rotated in the plane of the module by a *stereo* angle of  
 326 100 mrad; the hits from these two modules, known as *stereo hits*, are combined to  
 327 provide a measurement of the second coordinate ( $z$  in the barrel and  $r$  on the disks)  
 328 allowing the reconstruction of hit positions in 3-D.

329  
 330 The outer tracker region is composed of the tracker outer barrel (TOB) and the  
 331 tracker endcaps (TEC). The six layers of the TOB offer coverage in the region  $r > 55$

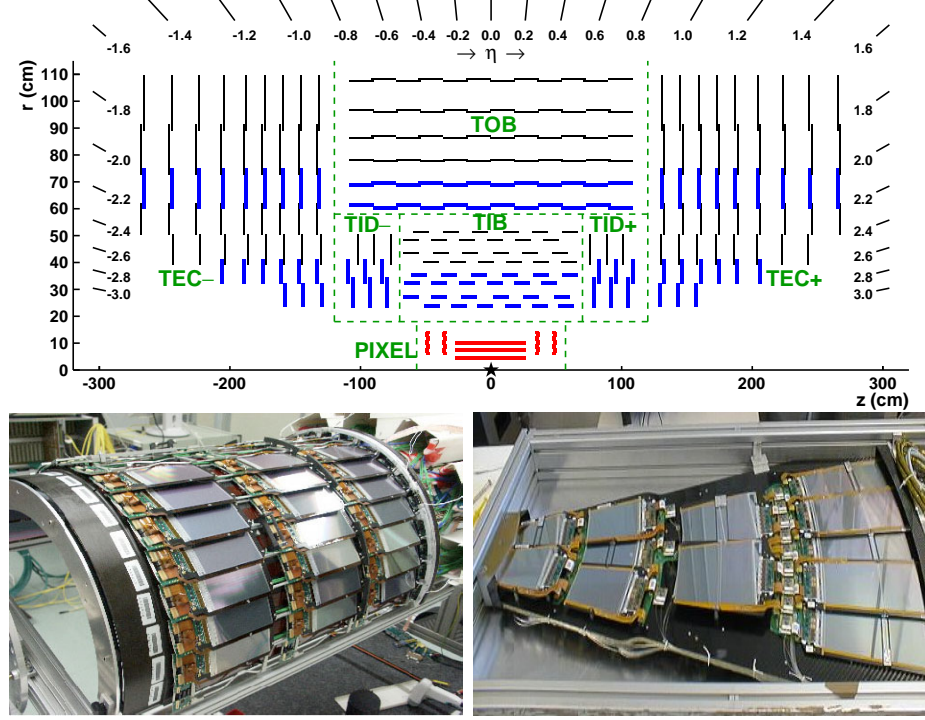


**Figure 3.12:** Top: CMS Silicon Strip Tracker (SST) schematic view. The SST is composed of the tracker inner barrel (TIB), the tracker inner disks (TID), the tracker outer barrel (TOB) and the tracker endcaps (TEC). Each part is made of silicon strip modules; the modules in blue represent two modules mounted back-to-back and rotated in the plane of the module by a stereo angle of 120 mrad in order to provide a 3-D reconstruction of the hit positions. Bottom: pictures of the TIB (left) and TEC (right) modules [71–73].

332 cm and  $|z| < 118$  cm, while the 9 disks of the TEC cover the region  $124 < |z| < 282$   
 333 cm. The resolution offered by the outer tracker is about  $13\text{--}38 \mu\text{m}$  in the  $r\phi$  position  
 334 measurement. The inner four TEC disks use silicon sensors  $320 \mu\text{m}$  thick; those in  
 335 the TOB and the outer three TEC disks use silicon sensors of  $500 \mu\text{m}$  thickness. The  
 336 silicon strips run parallel to the  $z$ -axis and the distance between strips varies from 80  
 337  $\mu\text{m}$  in the inner TIB layers to  $183 \mu\text{m}$  in the inner TOB layers; in the endcaps the  
 338 wedge-shaped sensors with radial strips, whose pitch range between  $81 \mu\text{m}$  at small  
 339 radii and  $205 \mu\text{m}$  at large radii.

340

341 The whole SST has 15148 silicon modules, 9.3 million silicon strips and cover a total

342 active area of about  $198 \text{ m}^2$ .

### 343 3.3.4 Electromagnetic calorimeter

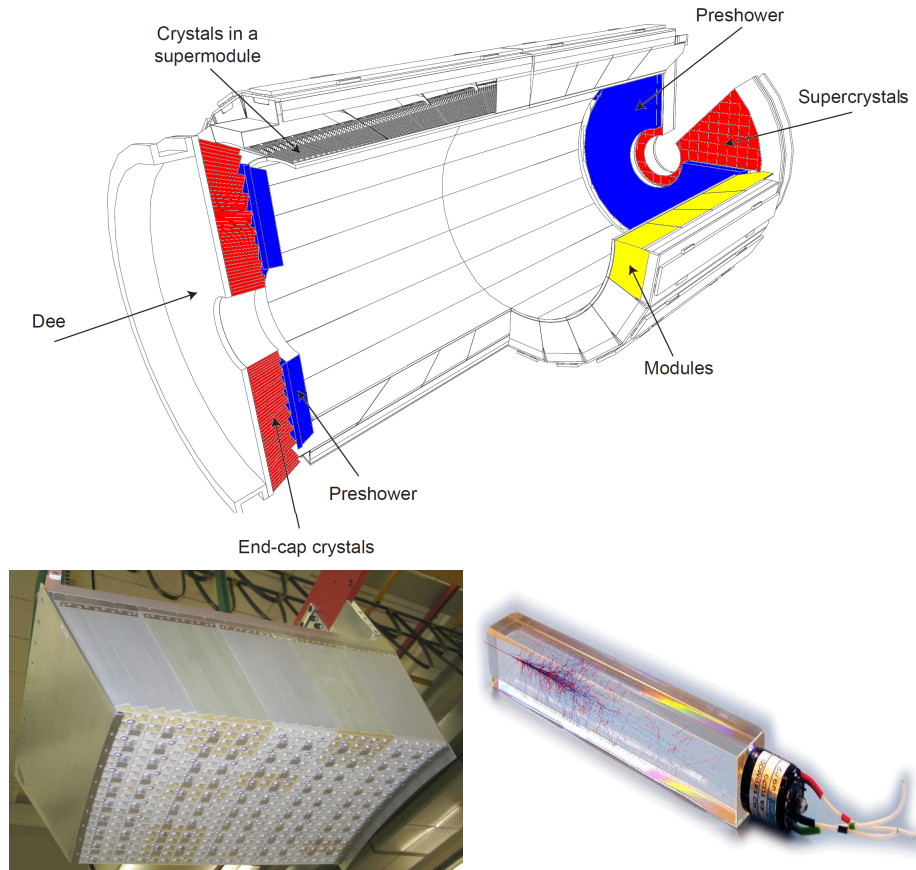


**Figure 3.13:** Top: CMS ECAL schematic view. Bottom: Module equipped with the crystals (left); ECAL crystal(right).

344 The CMS electromagnetic calorimeter (ECAL) is designed to measure the energy of  
 345 electrons and photons. It is composed of 75848 lead tungstate crystals which have a  
 346 short radiation length (0.89 cm) and fast response, since 80% of the light is emitted  
 347 within 25 ns; however, they are combined with Avalanche photodiodes (APDs) as  
 348 photodetectors given that crystals themselves have a low light yield ( $30\gamma/\text{MeV}$ ). A

349 schematic view of the ECAL is shown in Figure 3.13.

350

351 Energy is measured when electrons and photons are absorbed by the crystals which  
 352 generates an electromagnetic *shower*, as seen in bottom right picture of the Figure  
 353 3.13; the shower is seen as a *cluster* of energy which depending on the amount of en-  
 354 ergy deposited can involve several crystals. The ECAL barrel (EB) covers the region  
 355  $|\eta| < 1.479$ , using crystals of depth of 23 cm and  $2.2 \times 2.2 \text{ cm}^2$  transverse section;  
 356 the ECAL endcap (EE) covers the region  $1.479 < |\eta| < 3.0$  using crystals of depth  
 357 22 cm and transverse section of  $2.86 \times 2.86 \text{ cm}^2$ ; the photodetectors used are vacuum  
 358 phototriodes (VPTs). Each EE is divided in two structures called *Dees*.

359

360 In front of the EE, it is installed the preshower detector (ES) which covers the region  
 361  $1.653 < |\eta| < 2.6$ . The ES provides a precise measurement of the position of electro-  
 362 magnetic showers, which allows to distinguish electrons and photons signals from  $\pi^0$   
 363 decay signals. The ES is composed of a layer of lead absorber followed by a layer of  
 364 plastic scintillators

### 365 3.3.5 Hadronic calorimeter

366 Hadrons are not absorbed by the ECAL but by the hadron calorimeter (HCAL),  
 367 which is made of a combination of alternating brass absorber layers and silicon photo-  
 368 multiplier(SiPM) layers; therefore, particles passing through the scintillator material  
 369 produce showers, as in the ECAL, as a result of the inelastic scattering of the hadrons  
 370 with the detector material. Since the particles are not absorbed in the scintillator,  
 371 their energy is sampled; therefore the total energy is not measured but estimated from  
 372 the energy clusters, which reduce the resolution of the detector. Brass was chosen

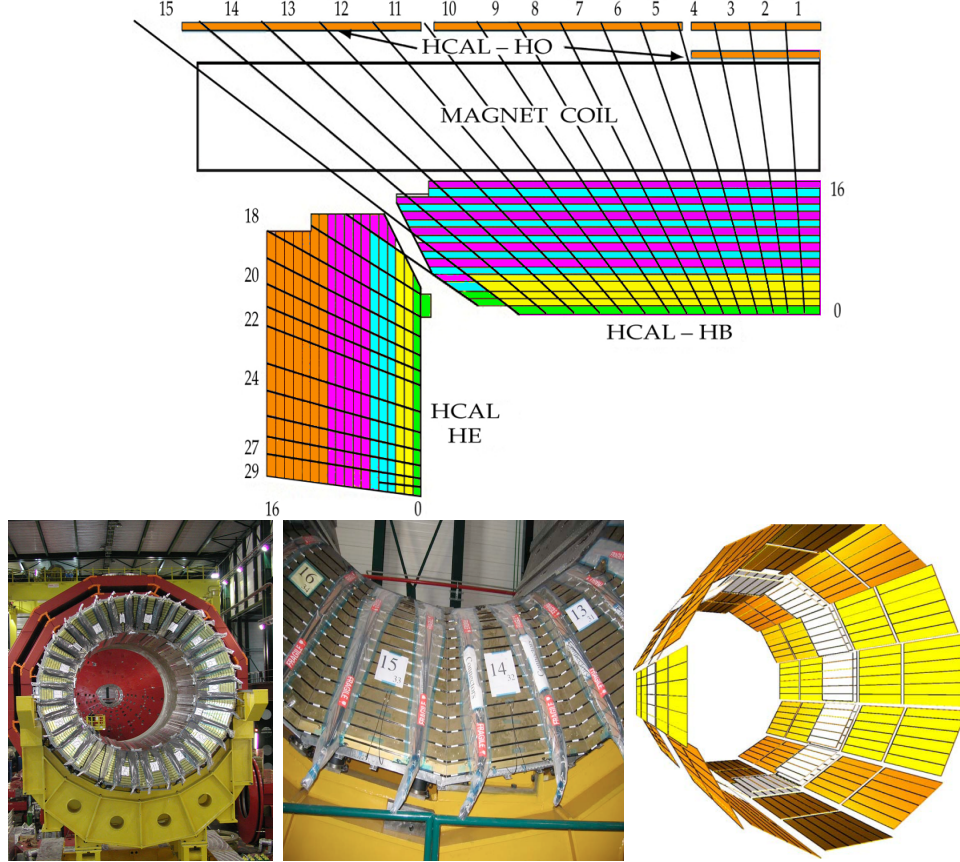


**Figure 3.14:** Top: CMS HCAL schematic view, the colors indicate the layers that are grouped into the same readout channels. Bottom: picture of a section of the HB; the absorber material is the golden region and scintillators are placed in between the absorber material (left and center). Schematic view of the HO (right). [74,75]

373 as the absorber material due to its short interaction length ( $\lambda_I = 16.42\text{cm}$ ) and its  
 374 non-magnetivity. Figure 3.14 shows a schematic view of the CMS HCAL.

375

376 The HCAL is divided into four sections; the Hadron Barrel (HB), the Hadron Outer  
 377 (HO), the Hadron Endcap (HE) and the Hadron Forward (HF) sections. The HB  
 378 covers the region  $0 < |\eta| < 1.4$ , while the HE covers the region  $1.3 < |\eta| < 3.0$ . The HF,  
 379 made of quartz fiber scintillator and steel as absorption material, covers the forward  
 380 region  $3.0 < |\eta| < 5.2$ . Both the HB and HF are located inside the solenoid. The HO

381 is placed outside the magnet as an additional layer of scintillators with the purpose  
 382 of measure the energy tails of particles passing through the HB and the magnet (see  
 383 Figure 3.14 top and bottom right). The upgrades made to the HCAL during the  
 384 technical stop 2016-2017 consisted in the replacement of the photo transducer, in  
 385 order to improve the efficiency.

386 **3.3.6 Superconducting solenoid magnet**

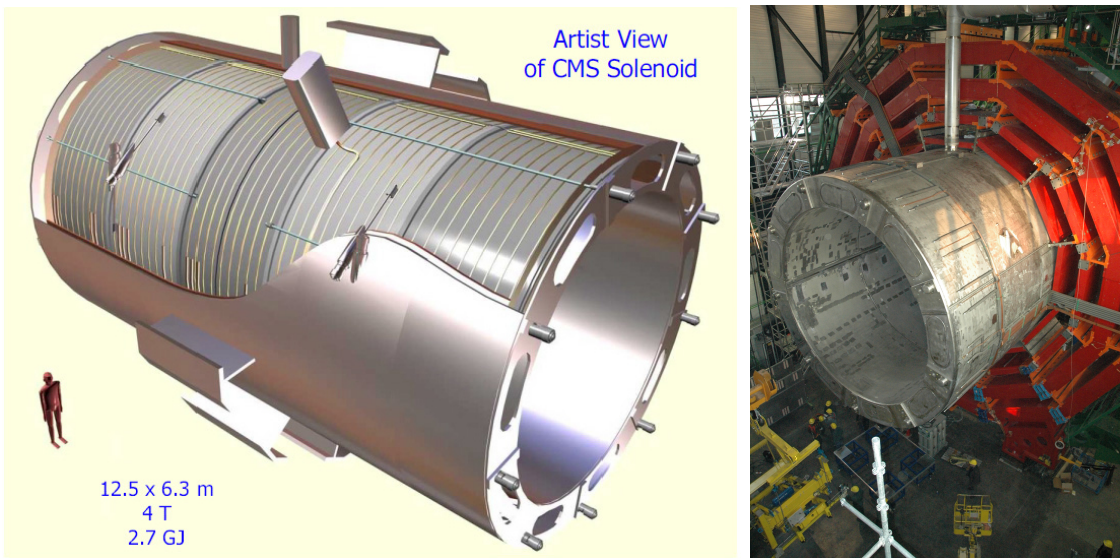


**Figure 3.15:** Artistic representation of the CMS solenoid magnet(left). The magnet is supported on an iron yoke (right) which also serves as the house of the muon detector and as mechanical support for the whole CMS detector [69].

387 The superconducting magnet installed in the CMS detector is designed to provide  
 388 an intense and highly uniform magnetic field in the central part of the detector. In  
 389 fact, the tracking system takes advantage of the bending power of the magnetic field  
 390 to measure with precision the momentum of the particles that traverse it; the unam-  
 391 biguous determination of the sign for high momentum muons was a driven principle  
 392 during the design of the magnet. The magnet has a diameter of 6.3 m, a length of 12.5  
 393 m and a cold mass of 220 t; the generated magnetic field reaches a strength of 3.8T.

394 Since it is made of Ni-Tb superconducting cable it has to operate at a temperature  
 395 of 4.7 K by using a helium cryogenic system; the current circulating in the cables  
 396 reaches 18800 A under normal running conditions. The left side of Figure 3.15 shows  
 397 an artistic view of the CMS magnet, while the right side shows a transverse view of  
 398 the cold mass where the winding structure is visible.

399

400 The yoke (see Figure 3.15), composed of 5 barrel wheels and 6 endcap disks made  
 401 of iron, serves not only as the media for magnetic flux return but also provides the  
 402 house for the muon detector system and structural stability to the full detector.

### 403 3.3.7 Muon system

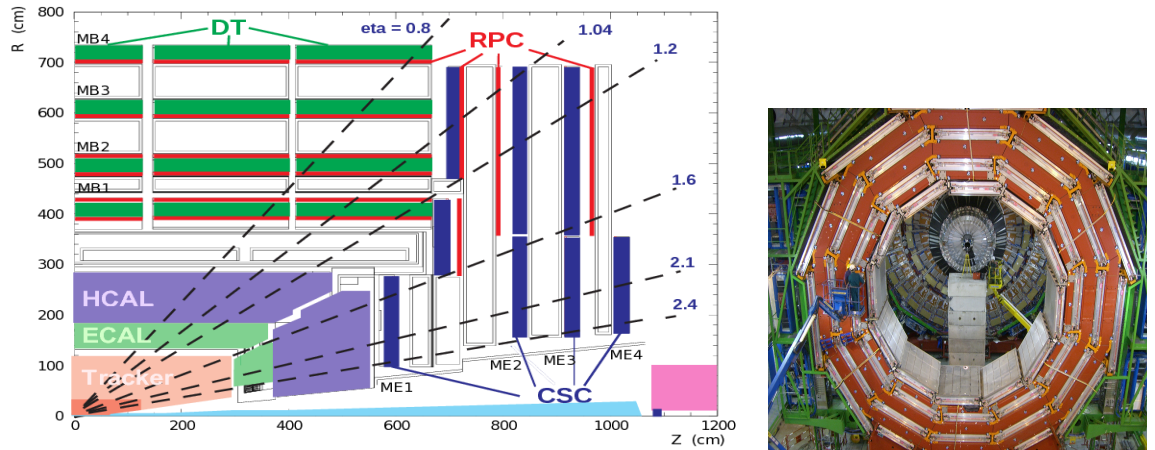


**Figure 3.16:** Left: CMS muon system schematic view; Right: one of the yoke rings with the muon DTs and RPCs installed; in the back it is possible to see the muon endcap [76].

404 Muons are the only charged particles able to pass through all the CMS detector due  
 405 to their low ionization energy loss; thus, muons can be separated easily from the  
 406 high amount of particles produced in a  $pp$  collision. Also, muons are expected to be  
 407 produced in the decay of several new particles; therefore, a good detection of muons

408 was on the leading principles when designing the CMS detector.

409

410 The CMS muon detection system (muon spectrometer) is embedded in the return  
411 yoke as seen in Figure 3.16. It is composed of three different detector types, the drift  
412 tube chambers (DT), Cathode strip chambers (CSC), and resistive plate chambers  
413 (RPC); DT are located in the central region  $\eta < 1.2$  arranged in four layers of drift  
414 chambers filled with an Ar/CO<sub>2</sub> gas mixture.

415

416 The muon endcaps are made of CSCs covering the region  $\eta < 2.4$  and filled with a  
417 mixture of Ar/CO<sub>2</sub>/CF<sub>4</sub>. The reason behind using a different detector type lies on  
418 the different conditions in the forward region like the higher muon rate and higher  
419 residual magnetic field compared to the central region.

420

421 The third type of detector used in the muon system is a set of four disks of RPCs  
422 working in avalanche mode. The RPCs provide good spatial and time resolutions.  
423 The track of *high – p<sub>T</sub>* muon candidates is built combining information from the  
424 tracking system and the signal from up to six RPCs and four DT chambers.  
425 The muon tracks are reconstructed from the hits in the several layers of the muon  
426 system.

### 427 **3.3.8 CMS trigger system**

428 Under normal conditions, CMS expects *pp* collisions every 25 ns, i.e., an interaction  
429 rate of 40 MHz for which it is not possible to store the recorded data in full. In order  
430 to handle this high event rate data, an online event selection, known as triggering, is  
431 performed; triggering reduce the event rate to 100 Hz for storage and further offline

432 analysis.

433

434 The trigger system starts with a reduction of the event rate to 100 kHz in the so-  
 435 called *level 1 trigger (L1)*. L1 is based on dedicated programmable hardware like  
 436 Field Programmable Gate Arrays (FPGAs) and Application Specific Integrated Cir-  
 437 cuits (ASICs), partly located in the detector itself; another portion is located in the  
 438 CMS under-ground cavern. Hit patterns information from the muon chambers and  
 439 the energy deposits in the calorimeter are used to decide if an event is accepted or  
 440 rejected, according to selection requirements previously defined, which reflect the in-  
 441 teresting physics processes. Figure 3.17 shows the L1 trigger architecture.

442

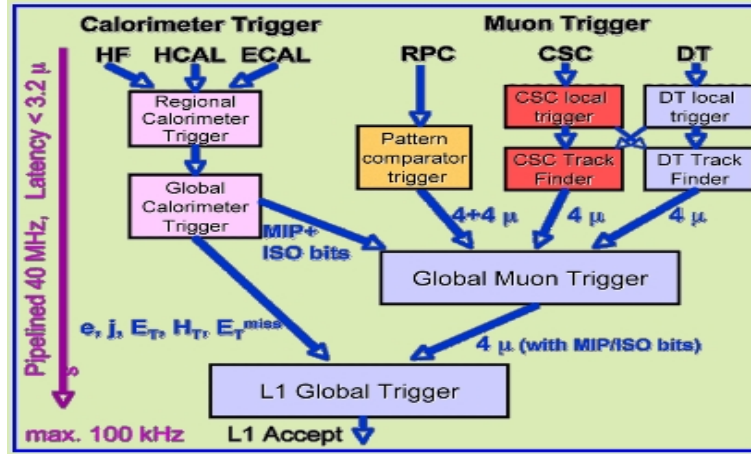


**Figure 3.17:** CMS Level-1 trigger architecture [77].

443 The second stage in the trigger system is called *high-level trigger (HLT)*; events ac-  
 444 cepted by L1 are passed to HLT in order to make an initial reconstruction of them.  
 445 HLT is software based and runs on a dedicated server farm, using selection algo-  
 446 rithms and high-level object definitions; the event rate at HLT is reduced to 100 Hz.  
 447 The first HLT stage takes information from the muon detectors and the calorimeters  
 448 to make the initial object reconstruction; in the next HLT stage, information from

449 the pixel and strip detectors is used to do first fast-tracking and then full tracking  
450 online. This initial object reconstruction is used in further steps of the trigger system.

451

452 Events and preliminary reconstructed physics objects from HLT are sent to be fully  
453 reconstructed at the CERN computing center. Again, the pixel detector information  
454 provides high-quality seeds for the track reconstruction algorithm offline, primary ver-  
455 tex reconstruction, electron and photon identification, muon reconstruction,  $\tau$  iden-  
456 tification, and b-tagging. After full reconstruction, data sets are made available for  
457 offline analyses.

458

459 During the 2016-2017 technical stop, the L1 system was updated in order to improve  
460 the physics object identification by improving the algorithms and accounting for the  
461 increasing pile-up scenario.

### 462 **3.3.9 CMS computing**

463 After the data, coming from the experiment, are processed at several levels, they have  
464 to be stored and made available for further analysis; in order to cope all the tasks  
465 implied in the offline data processing, like transfer, simulation, reconstruction and  
466 reprocessing, among others, a big computing power is required. The CMS computing  
467 system is based on the distributed architecture concept, where users of the system  
468 and physical computer centers are distributed worldwide and interconnected by high-  
469 speed networks.

470 The worldwide LHC computing grid (WLCG) is the mechanism used to provide that  
471 distributed environment. WLCG is a tiered structure connecting computing centers  
472 around the world, which provides the necessary storage and computing facilities. The

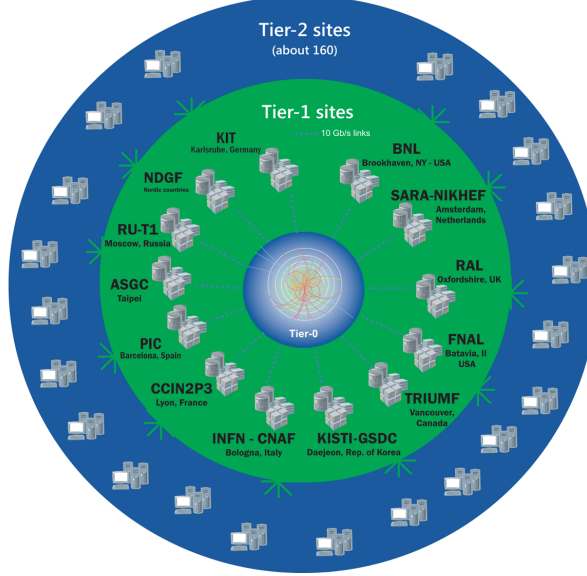


**Figure 3.18:** WLCG structure. The primary computer centers (Tier-0) are located at CERN (data center) and at the Wigner datacenter in Budapest. Tier-1 is composed of 13 centers and Tier-2 is composed of about 160 centers. [78].

473 primary computing centers of the WLCG are located at the CERN and the Wigner  
 474 datacenter in Budapest and are known as Tier-0 as shown in Figure 3.18. The main  
 475 responsibilities for each tier level are [78]

- 476     • **Tier-0:** initial reconstruction of recorded events and storage of the resulting  
       477 datasets, the distribution of raw data to the Tier-1 centers.
- 478     • **Tier-1:** provide storage capacity, support for the Grid, safe-keeping of a pro-  
       479 portional share of raw and reconstructed data, large-scale reprocessing and safe-  
       480 keeping of corresponding output, generation of simulated events, distribution  
       481 of data to Tier 2s, safe-keeping of a share of simulated data produced at these  
       482 Tier 2s.
- 483     • **Tier-2:** store sufficient data and provide adequate computing power for specific  
       484 analysis tasks, provide analysis requirements and proportional share of simu-  
       485 lated event production and reconstruction.

486 Aside from the general computing strategy to manage the huge amount of data pro-  
 487 duced by experiments, CMS uses a framework to perform a variety of processing,  
 488 selection and analysis tasks. The central concept of the CMS data model referred to  
 489 as *event data model* (EDM) is the *Event*; therefore, an event is the unit that contains  
 490 the information from a single bunch crossing as well as any data derived from that  
 491 information like the reconstructed objects, the details under which additional data  
 492 are derived.

493

494 Events are passed as the input to the *physics modules* that obtain information from  
 495 them and create new one; for instance, *event data producers* add new data into the  
 496 events, *analyzers* produce an information summary from an event set, *filters* perform  
 497 selection and triggering.

498

499 CMS uses several event formats with different levels of detail and precision

500 • **Raw format:** events in this format contain the full recorded information from  
 501 the detector as well as trigger decision and other metadata. An extended version  
 502 of raw data is used to store information from the CMS Monte Carlo simulation  
 503 tools. Raw data are stored permanently, occupying about 2MB/event

504 • **RECO format:** events in this format correspond to raw data that have been  
 505 submitted to reconstruction algorithms like primary and secondary vertex re-  
 506 construction, particle ID, track-finding. RECO events contain physical objects  
 507 and all the information used to reconstruct them; average size is about 0.5  
 508 MB/event.

509 • **AOD format:** Analysis Object Data (AOD) is the data format used in the  
 510 physics analyses given that it contains the parameters describing the high-level

511        physics objects in addition to enough information to allow a kinematic refitting if  
 512        needed. AOD events are filtered versions of the RECO events to which skimming  
 513        or other kind processes have been applied. Requires about 100 kB/event.

514        • **Non-event data** are data needed to interpret and reconstruct events. Some  
 515        of the non-event data used by CMS contains information about the detector  
 516        contraction and condition data like calibrations, alignment, and detector status.

517        Figure 3.19 shows the data flow scheme between CMS detector and hardware tiers.

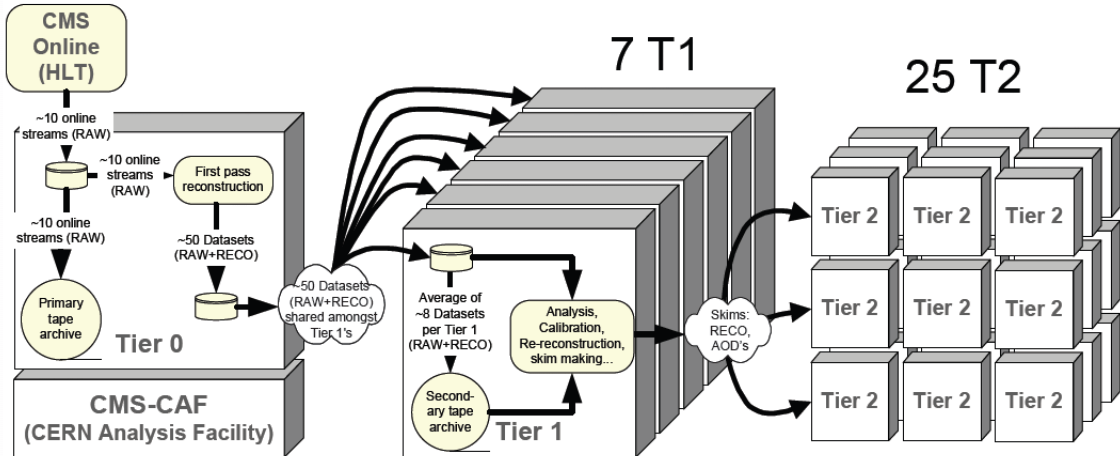


**Figure 3.19:** Data flow from CMS detector through hardware Tiers.

518        The whole collection of software built as a framework is referred to as *CMSSW*. This  
 519        framework provides the services needed by the simulation, calibration and alignment,  
 520        and reconstruction modules that process event data, so that physicists can perform  
 521        analysis. The CMSSW event processing model is composed of one executable, called  
 522        cmsRun, and several plug-in modules which contains all the tools (calibration, recon-  
 523        struction algorithms) needed to process an event. The same executable is used for  
 524        both detector and Monte Carlo data [79].

525 **Chapter 4**

526 **Event generation, simulation and  
527 reconstruction**

528 The process of analyzing data recorded by the CMS experiment involves several stages  
529 where the data are processed in order to interpret the information provided by all  
530 the detection systems; in those stages, the particles produced after the  $pp$  collision  
531 are identified by reconstructing their trajectories and measuring their features. In  
532 addition, the SM provides a set of predictions that have to be compared with the  
533 experimental results; however, in most of the cases, theoretical predictions are not  
534 directly comparable to experimental results due to the diverse source of uncertainties  
535 introduced by the experimental setup and theoretical approximations, among others.

536

537 The strategy to face these conditions consists in using statistical methods imple-  
538 mented in computational algorithms to produce numerical results that can be con-  
539 trasted with the experimental results. These computational algorithms are commonly  
540 known as Monte Carlo (MC) methods and, in the case of particle physics, they are  
541 designed to apply the SM rules and produce predictions about the physical observ-

ables measured in the experiments. Since particle physics is governed by quantum mechanics principles, predictions are not allowed from single events; therefore, a high number of events are *generated* and predictions are produced in the form of statistical distributions for the observables. Effects of the detector presence are included in the predictions by introducing simulations of the detector itself.

547

548 This chapter presents a description of the event generation strategy and the tools  
 549 used to perform the detector simulation and physics objects reconstruction. A com-  
 550 prehensive review of event generators for LHC physics can be found in Reference [80]  
 551 on which this chapter is based.

## 552 4.1 Event generation

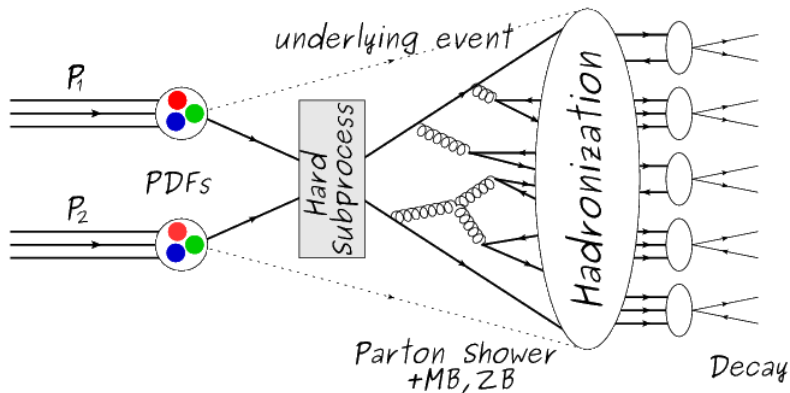


**Figure 4.1:** Event generation process. The actual interaction is generated in the hard subprocess. The parton shower describes the evolution of the partons from the hard subprocess. Modified from Reference [81].

553 The event generation is intended to create events that mimic the behavior of actual  
 554 events produced in collisions; they obey a sequence of steps from the particles collision  
 555 hard process to the decay process into the final state. Figure 4.1 shows a schematic  
 556 view of the event generation process; the fact that the full process can be treated as

557 several independent steps is motivated by the QCD factorization theorem.

558

559 Generation starts by taking into account the PDFs of the incoming particles. Event  
 560 generators offer the option to chose from several PDF sets depending on the particu-  
 561 lar process under simulation<sup>1</sup>; in the following,  $pp$  collisions will be considered. The  
 562 *hard subprocess* describes the actual interaction between partons from the incoming  
 563 protons; it is represented by the matrix element connecting the initial and final states  
 564 of the interaction. Normally, the matrix element can be written as a sum over Feyn-  
 565 man diagrams and consider interferences between terms in the summation. During  
 566 the generation of the hard subprocess, the production cross section is calculated.

567

568 The order to which the cross section is calculated depends on the order of the Feyn-  
 569 man diagrams involved in the calculation; therefore, radiative corrections are included  
 570 by considering a higher order Feynman diagrams where QCD radiation dominates.  
 571 Currently, cross sections calculated to LO do not offer a satisfactory description of the  
 572 processes, i.e., the results are only reliable for the shape of distributions; therefore,  
 573 NLO calculations have to be performed with the implication that the computing time  
 574 needed is highly increased.

575

576 The final parton content of the hard subprocess is subjected to the *parton shower*  
 577 which generates the gluon radiation. Parton shower evolves the partons, i.e., glouns  
 578 split into quark-antiquark pairs and quarks with enough energy radiate gluons giv-  
 579 ing rise to further parton multiplication, following the DGLAP (Dokshitzer-Gribov-  
 580 Lipatov-Altarelli-Parisi) equations. Showering continues until the energy scale is low  
 581 enough to reach the non-perturbative limit.

---

<sup>1</sup> Tool in Reference [82] allows to plot different PDF sets under customizable conditions.

582

583 In the simulation of LHC processes that involve  $b$  quarks, like the single top quark  
 584 or Higgs associated production, it is needed to consider that the  $b$  quark is heavier  
 585 than the proton; hence, the QCD interaction description is made in two different  
 586 schemes [83]

587 • four-flavor (4F) scheme.  $b$  quarks appear only in the final state because they  
 588 are heavier than the proton and therefore they can be produced only from the  
 589 splitting of a gluon into pairs or singly in association with a  $t$  quark in high  
 590 energy-scale interactions; furthermore, during the simulation, the  $b$ -PDFs are set  
 591 to zero. Calculations in this scheme are more complicated due to the presence  
 592 of the second  $b$  quark but the full kinematics is considered already at LO and  
 593 therefore the accuracy of the description is better.

594 • five-flavor (5F) scheme.  $b$  quarks are considered massless, therefore they can  
 595 appear in both initial and final states since they can now be part of the proton;  
 596 thus, during the simulation  $b$ -PDFs are not set to zero. In this scheme, calcu-  
 597 lations are simpler than in the 4F scheme and possible logarithmic divergences  
 598 are absorbed by the PDFs through the DGLAP evolution.

599 In this thesis, the  $tHq$  events are generated using the 4F scheme in order to reduce  
 600 uncertainties, while the  $tHW$  events are generated using the 5F scheme to eliminate  
 601 LO interference with  $t\bar{t}H$  process [48].

602

603 Partons involved in the  $pp$  collision are the focus of the simulation, however, the rest  
 604 of the partons inside the incoming protons are also affected because the remnants are  
 605 colored objects; also, multiple parton interactions can occur. The hadronization of  
 606 the remnants and multiple parton interactions are known as *underlying event* and it

607 has to be included in the simulation. In addition, multiple  $pp$  collisions in the same  
 608 bunch crossing (pile-up mentioned in 3.2) occurs, actually in two forms

609 • *in-time PU* which refers to multiple  $pp$  collision in the bunch crossing but that  
 610 are not considered as primary vertices.

611 • *Out-of-time PU* which refers to overlapping  $pp$  collisions from consecutive bunch  
 612 crossings; this can occur due to the time-delays in the detection systems where  
 613 information from one bunch crossing is assigned to the next or previous one.

614 While the underlying event effects are included in generation using generator-specific  
 615 tools, PU effects are added to the generation by overlaying Minimum-bias (MB) and  
 616 Zero-bias (ZB) events to the generated events. MB events are inelastic events se-  
 617 lected by using a loose trigger with as little bias as possible, therefore accepting a  
 618 large fraction of the overall inelastic event; ZB events correspond to random events  
 619 recorded by the detector when collisions are likely. MB models in-time PU and ZB  
 620 models out-of-time PU.

621

622 The next step in the generation process is called *hadronization*. Since particles with  
 623 a net color charge are not allowed to exits isolated, they have to recombine to form  
 624 bound states. This is precisely the process by which the partons resulting from the  
 625 parton shower arrange themselves as color singlets to form hadrons. At this step, the  
 626 energy-scale is low and the strong coupling constant is large, therefore hadronization  
 627 process is non-perturbative and the evolution of the partons is described using phe-  
 628 nomenological models. Most of the baryons and mesons produced in the hadronization  
 629 are unstable and hence they will decay in the detector.

630

631 The last step in the generation process corresponds to the decay of the unstable  
 632 particles generated during hadronization; it is also simulated in the hadronization  
 633 step, based on the known branching ratios.

## 634 4.2 Monte Carlo Event Generators.

635 The event generation described in the previous section has been implemented in  
 636 several software packages for which a brief description is given.

- 637 • **PYTHIA 8.** It is a program designed to perform the generation of high energy  
 638 physics events which describes the collisions between particles such as electrons  
 639 and protons. Several theories and models are implemented in it, in order to  
 640 describe physical aspects like hard and soft interaction, parton distributions,  
 641 initial and final-state parton showers, multiple parton interactions, beam rem-  
 642 nants, hadronization<sup>2</sup> and particle decay. Thanks to extensive testing, several  
 643 optimized parametrizations, known as *tunings*, have been defined in order to  
 644 improve the description of actual collisions to a high degree of precision; for  
 645 analysis at  $\sqrt{s} = 13$  TeV, the underline event CUETP8M1 tune is employed [85].  
 646 The calculation of the matrix element is performed at LO which is not enough  
 647 for the current required level of precision; therefore, pythia is often used for  
 648 parton shower, hadronization and decays, while other event generators are used  
 649 to generate the matrix element at NLO.

- 650 • **MadGraph5\_aMC@NLO.** MadGraph is a matrix element generator which  
 651 calculates the amplitudes for all contributing Feynman diagrams of a given pro-  
 652 cess but does not provide a parton shower while MC@NLO incorporates NLO

---

<sup>2</sup> based in the Lund string model [84]

653 QCD matrix elements consistently into a parton shower framework; thus, Mad-  
 654 Graph5\_aMC@NLO, as a merger of the two event generators MadGraph5 and  
 655 aMC@NLO, is an event generator capable to calculate tree-level and NLO cross  
 656 sections and perform the matching of those with the parton shower. It is one of  
 657 the most frequently used matrix element generators; however, it has the partic-  
 658 ular feature of the presence of negative event weights which reduce the number  
 659 of events used to reproduce the properties of the objects generated [86].

660

661 • **POWHEG.** It is an NLO matrix element generator where the hardest emis-  
 662 sion of color charged particles is generated in such a way that the negative event  
 663 weights issue of MadGraph5\_aMC@NLO is overcome; however, the method re-  
 664 quires an interface with  $p_T$ -ordered parton shower or a parton shower generator  
 665 where this highest emission can be vetoed in order to avoid double counting of  
 666 this highest-energetic emission. PYTHIA is a commonly matched to POWHEG  
 667 event generator [87].

668 Events resulting from the whole generation process are known as MC events.

### 669 4.3 CMS detector simulation.

670 After generation, MC events contain the physics of the collisions but they are not  
 671 ready to be compared to the events recorded by the experiment since these recorded  
 672 events correspond to the response of the detection systems to the interaction with  
 673 the particles traversing them. The simulation of the CMS detector has to be applied  
 674 on top of the event generation; it is simulated with a MC toolkit for the simulation  
 675 of particles passing through matter called Geant4 which is also able to simulate the

676 electronic signals that would be measured by all detectors inside CMS.

677

678 The simulation takes the generated particles contained in the MC events as input,  
679 makes them pass through the simulated geometry, and models physics processes that  
680 particles experience during their passage through matter. The full set of results from  
681 particle-matter interactions corresponds to the simulated hit which contains informa-  
682 tion about the energy loss, momentum and position. Particles of the input event are  
683 called *primary*, while the particles originating from GEANT4-modeled interactions of  
684 a primary particle with matter are called a *secondary*. Simulated hits are the input  
685 of subsequent modules that emulate the response of the detector readout system and  
686 triggers. The output from the emulated detection systems and triggers is known as  
687 digitization [88, 89].

688

689 The modeling of the CMS detector corresponds to the accurate modeling of the  
690 interaction among particles, the detector material, and the magnetic field. This  
691 simulation procedure includes the following standard steps

- 692     • Modeling of the Interaction Region.
- 693     • Modeling of the particle passage through the hierarchy of volumes that compose  
694        CMS detector and of the accompanying physics processes.
- 695     • Modeling of the effect of multiple interactions per beam crossing and/or the  
696        effect of events overlay ( Pile-Up simulation).
- 697     • Modeling of the detector's electronics response, signal shape, noise, calibration  
698        constants (digitization).

699 In addition to the full simulation, i.e., a detailed detector simulation, a faster simu-  
 700 lation (FastSim) have been developed, that may be used where much larger statistics  
 701 are required. In FastSim, detector material effects are parametrized and included in  
 702 the hits; those hits are used as input of the same higher-level algorithms<sup>3</sup> used to an-  
 703 alyze the recorded events. In this way, comparisons between fast and full simulations  
 704 can be performed [91].

705

706 After the full detector simulation, the output events can be directly compared to  
 707 events actually recorded in the CMS detector. The collection of MC events that  
 708 reproduces the expected physics for a given process is known as MC sample.

## 709 **4.4 Event reconstruction.**

710 The CMS experiment use the *particle-flow event reconstruction algorithm (PF)* to do  
 711 the reconstruction of particles produced in  $pp$  collisions. Next sections will present  
 712 a basic description of the *Elements* used by PF (tracker tracks, energy clusters, and  
 713 muon tracks), based in the References [92, 93] where more detailed descriptions can  
 714 be found.

### 715 **4.4.1 Particle-Flow Algorithm.**

716 Each of the several sub detection systems of the CMS detector is dedicated to identify  
 717 an specific type of particles, i.e., photons and electrons are absorbed by the ECAL  
 718 and their reconstruction is based on ECAL information; hadrons are reconstructed  
 719 from clusters in the HCAL while muons are reconstructed from hits in the muon

---

<sup>3</sup> track fitting, calorimeter clustering, b tagging, electron identification, jet reconstruction and calibration, trigger algorithms which will be considered in the next sections

chambers. PF is designed to correlate signals from all the detector layers (tracks and energy clusters) in order to reconstruct and identify each final state particle and its properties as sketched in Figure 4.2.

723

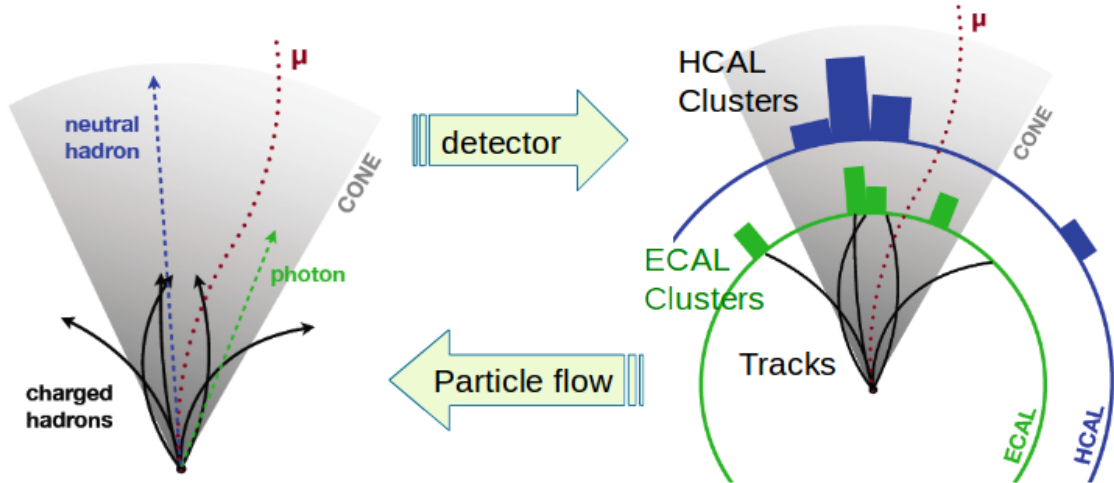


**Figure 4.2:** Particle flow algorithm. Information from the several CMS detection systems is provided as input to the algorithm which then combines it to identify and reconstruct all the particles in the final state and their properties. Reconstruction of simulated events is also performed by providing information from MC samples, detector and trigger simulation [94].

For instance, a charged hadron is identified by a geometrical connection, known as *link*, between one or more calorimeter clusters and a track in the tracker, provided there are no hits in the muon system; combining several measurements allows a better determination of the energy and charge sign of the charged hadron.

### 728 Charged-particle track reconstruction.

The strategy used by PF in order to reconstruct tracks is called *Iterative Tracking* which occurs in four steps

- 731 • Seed generation where initial track candidates are found by looking for a combination of hits in the pixel detector, strip tracker, and muon chambers. In total

733 ten iterations are performed, each one with a different seeding requirement.  
 734 Seeds are used to estimate the trajectory parameters and uncertainties at the  
 735 time of the full track reconstruction. Seeds are also considered track candidates.

- 736     • Track finding using a tracking software known as Combinatorial Track Finder  
 737         (CTF) [95]. The seed trajectories are extrapolated along the expected flight  
 738         path of a charged particle, in agreement to the trajectory parameters obtained  
 739         in the first step, in an attempt to find additional hits that can be assigned to  
 740         the track candidates.
- 741     • Track-fitting where the found tracks are passed as input to a module which  
 742         provides the best estimate of the parameters of each trajectory.
- 743     • Track selection where track candidates are submitted to a selection which dis-  
 744         cards those that fail a set of defined quality criteria.

745 Iterations differ in the seeding configuration and the final track selection as elaborated  
 746 in References [92, 93]. In the first iteration, high  $p_T$  tracks and tracks produced near  
 747 to the interaction region are identified and those hits are masked thereby reducing  
 748 the combinatorial complexity. Next, iterations search for more complicated tracks,  
 749 like low  $p_T$  tracks and tracks from b hadron decays, which tend to be displaced from  
 750 the interaction region.

### 751 **Vertex reconstruction.**

752 During the track reconstruction, an extrapolation toward to the calorimeters is per-  
 753 formed in order to match energy deposits; that extrapolation is performed also toward  
 754 the beamline in order to find the origin of the track known as *vertex*. The vertex re-  
 755 construction is performed by selecting from the available reconstructed tracks, those

756 that are consistent with being originated in the interaction region where  $pp$  collisions  
 757 are produced. The selection involves a requirement on the number of tracker (pixel  
 758 and strip) hits and the goodness of the track fit.

759

760 Selected tracks are clustered using a *deterministic annealing algorithm* (DA)<sup>4</sup>. A set  
 761 of candidate vertices and their associated tracks, resulting from the DA, are then fit-  
 762 ted with an *adaptive vertex fitter* (AVF) to produce the best estimate of the vertices  
 763 locations.

764

765 The  $p_T$  of the tracks associated to a reconstructed vertex is added, squared and used  
 766 to organize the vertices; the vertex with the highest squared sum is designated as the  
 767 *primary vertex* (PV) while the rest are designated as PU vertices.

### 768 Calorimeter clustering.

769 After traversing the CMS tracker system, electrons, photons and hadrons deposit their  
 770 energy in the ECAL and HCAL cells. The PF clustering algorithm aims to provide  
 771 a high detection efficiency even for low-energy particles and an efficient distinction  
 772 between close energy deposits. The clustering runs independently in the ECAL barrel  
 773 and endcaps, HCAL barrel and endcaps, and the two preshower layers, following two  
 774 steps

- 775     • cells with an energy larger than a given seed threshold and larger than the energy  
 776       of the neighboring cells are identified as cluster seeds. The neighbor cells are  
 777       those that either share a side with the cluster seed candidate, or the eight closest  
 778       cells including cells that only share a corner with the seed candidate.

---

<sup>4</sup> DA algorithm and AVF are described in detail in References [97, 98]

779       • cells with at least a corner in common with a cell already in the cluster seed  
 780           and with an energy above a cell threshold are grouped into topological clusters.

781     Clusters formed in this way are known as *particle-flow clusters*. With this clustering  
 782     strategy, it is possible to detect and measure the energy and direction of photons and  
 783     neutral hadrons as well as differentiate these neutral particles from the charged hadron  
 784     energy deposits. In cases involving charged hadrons for which the track parameters  
 785     are not determined accurately, for instance, low-quality and high- $p_T$  tracks, clustering  
 786     helps in the energy measurements.

787     **Electron track reconstruction.**

788     Although the charged-particle track reconstruction described above works for elec-  
 789     trons, they lose a significant fraction of their energy via bremsstrahlung photon radi-  
 790     ation before reaching the ECAL; thus, the reconstruction performance depends on the  
 791     ability to measure also the radiated energy. The reconstruction strategy, in this case,  
 792     requires information from the tracking system and from the ECAL. Bremsstrahlung  
 793     photons are emitted at similar  $\eta$  values to that of the electron but at different values  
 794     of  $\phi$ ; therefore, the radiated energy can be recovered by grouping ECAL clusters in a  
 795      $\eta$  window over a range of  $\phi$  around the electron direction. The group is called ECAL  
 796     supercluster.

797  
 798     Electron candidates from the track-seeding and ECAL super clustering are merged  
 799     into a single collection which is submitted to a full electron tracking fit with a  
 800     Gaussian-sum filter (GSF) [96]. The electron track and its associated ECAL su-  
 801     percluster form a *particle-flow electron*.

802 **Muon track reconstruction.**

803 Given that the CMS detector is equipped with a muon spectrometer capable to iden-  
 804 tify and measure the momentum of the muons traversing it, the muon reconstruction  
 805 is not specific to PF; therefore, three different muon types are defined

- 806     • *Standalone muon.* A clustering on the DTs or CSCs hits is performed to form  
   807       track segments; those segments are used as seeds for the reconstruction in the  
   808       muon spectrometer. All DTs, CSCs, and RPCs hits along the muon trajectory  
   809       are combined and fitted to form the full track. The fitting output is called a  
   810       *standalone-muon track*.
- 811     • *Tracker muon.* Each track in the inner tracker with  $p_T$  larger than 0.5 GeV and  
   812       a total momentum  $p$  larger than 2.5 GeV is extrapolated to the muon system.  
   813       A *tracker muon track* corresponds to a extrapolated track that matches at least  
   814       one muon segment.
- 815     • *Global muon.* When tracks in the inner tracker (inner tracks) and standalone-  
   816       muon tracks are matched and turn out being compatibles, their hits are com-  
   817       bined and fitted to form a *global-muon track*.

818 Global muons sharing the same inner track with tracker muons are merged into a  
 819 single candidate. PF muon identification uses the muon energy deposits in ECAL,  
 820 HCAL, and HO associated with the muon track to improve the muon identification.

821 **Particle identification and reconstruction.**

822 PF elements are connected by a linker algorithm that tests the connection between any  
 823 pair of elements; if they are found to be linked, a geometrical distance that quantifies  
 824 the quality of the link is assigned. Two elements may be linked indirectly through

825 common elements. Linked elements form *PF blocks* and each PF block may contain  
 826 elements originating in one or more particles. Links can be established between  
 827 tracks, between calorimeter clusters, and between tracks and calorimeter clusters.  
 828 The identification and reconstruction start with a PF block and proceed as follows

829     • Muons. An *isolated global muon* is identified by evaluating the presence of  
   830       inner track and energy deposits close to the global muon track in the  $(\eta, \phi)$   
   831       plane, i.e., in a particular point of the global muon track, inner tracks and  
   832       energy deposits are sought within a radius of  $\Delta R = 0.3$  (see eqn. 3.7) from the  
   833       muon track; if they exit and the  $p_T$  of the found track added to the  $E_T$  of the  
   834       found energy deposit does not exceed 10% of the muon  $p_T$  then the global muon  
   835       is an isolated global muon. This isolation condition is stringent enough to reject  
   836       hadrons misidentified as muons.

837     *Non-isolated global muons* are identified using additional selection requirements  
   838       on the number of track segments in the muon system and energy deposits along  
   839       the muon track. Muons inside jets are identified with more stringent criteria  
   840       in isolation and momentum as described in Reference [99]. The PF elements  
   841       associated with an identified muon are masked from the PF block.

842     • Electrons are identified and reconstructed as described above plus some addi-  
   843       tional requirements on fourteen variables like the amount of energy radiated,  
   844       the distance between the extrapolated track position at the ECAL and the po-  
   845       sition of the associated ECAL supercluster, among others, which are combined  
   846       in an specialized multivariate analysis strategy that improves the electron iden-  
   847       tification. Tracks and clusters used to identify and reconstruct electrons are  
   848       masked in the PF block.

- 849     ● Isolated photons are identified from ECAL superclusters with  $E_T$  larger than 10  
850           GeV, for which the energy deposited at a distance of 0.15, from the supercluster  
851           position on the  $(\eta,\phi)$  plane, does not exceed 10% of the supercluster energy;  
852           note that this is an isolation requirement. In addition, there must not be links  
853           to tracks. Clusters involved in the identification and reconstruction are masked  
854           in the PF block.
- 855     ● Bremsstrahlung photons and prompt photons tend to convert to electron-positron  
856           pairs inside the tracker, therefore, a dedicated finder algorithm is used to link  
857           tracks that seem to originate from a photon conversion; in case those two tracks  
858           are compatible with the direction of a bremsstrahlung photon, they are also  
859           linked to the original electron track. Photon conversion tracks are also masked  
860           in the PF block.
- 861     ● The remaining elements in the PF block are used to identify hadrons. In the  
862           region  $|\eta| \leq 2.5$ , neutral hadrons are identified with HCAL clusters not linked  
863           to any track while photons from neutral pion decays are identified with ECAL  
864           clusters without links to tracks. In the region  $|\eta| > 2.5$  ECAL clusters linked to  
865           HCAL clusters are identified with a charged or neutral hadron shower; ECAL  
866           clusters with no links are identified with photons. HCAL clusters not used yet,  
867           are linked to one or more unlinked tracks and to an unlinked ECAL in order to  
868           reconstruct charged-hadrons or a combination of photons and neutral hadrons  
869           according to certain conditions on the calibrated calorimetric energy.
- 870     ● Charged-particle tracks may be liked together when they converge to a *sec-  
871           ondary vertex (SV)* displaced from the interaction point where the PV and PU  
872           vertices are reconstructed; at least three tracks are needed in that case, of which  
873           at most one has to be an incoming track with hits in tracker region between a

874 PV and the SV.

875

876 The linker algorithm, as well as the whole PF algorithm, has been validated and  
 877 commissioned; results from that validation are presented in the Reference [92].

878 **Jet reconstruction.**

879 Quarks and gluons may be produced in the  $pp$  collisions, therefore, their hadronization  
 880 will be seen in the detector as a shower of hadrons and their decay products in the  
 881 form of a *jet*. The anti- $k_t$  algorithm [100] is used to perform the jet reconstruction  
 882 by clustering those PF particles within a cone (see Figure 4.3); previously, isolated  
 883 electrons, isolated muons, and charged particles associated with other interaction  
 884 vertices are excluded from the clustering.

885 The anti- $k_t$  algorithm proceeds in a sequential recombination of PF particles; the  
 886 distance between particles  $i$  and  $j$  ( $d_{ij}$ ) and the distance between particles and the  
 887 beam are defined as

$$d_{ij} = \min\left(\frac{1}{k_{ti}^2}, \frac{1}{k_{tj}^2}\right) \frac{\Delta_{ij}^2}{R^2}$$

$$d_{iB} = \frac{1}{k_{ti}^2} \quad (4.1)$$

888 where  $\Delta_{ij}^2 = (y_i - y_j)^2 + (\phi_i - \phi_j)^2$ ,  $k_{ti}, y_i$  and  $\phi_i$  are the transverse momentum, ra-  
 889 pidity and azimuth of particle  $i$  respectively and  $R$  is the called jet radius. For all  
 890 the remaining PF particles, after removing the isolated ones,  $d_{ij}$  and  $d_{iB}$  are calcu-  
 891 lated<sup>5</sup> and the smallest is identified; if it is a  $d_{ij}$ , particles  $i$  and  $j$  are replaced with

---

<sup>5</sup> Notice that this is a combinatorial calculation.

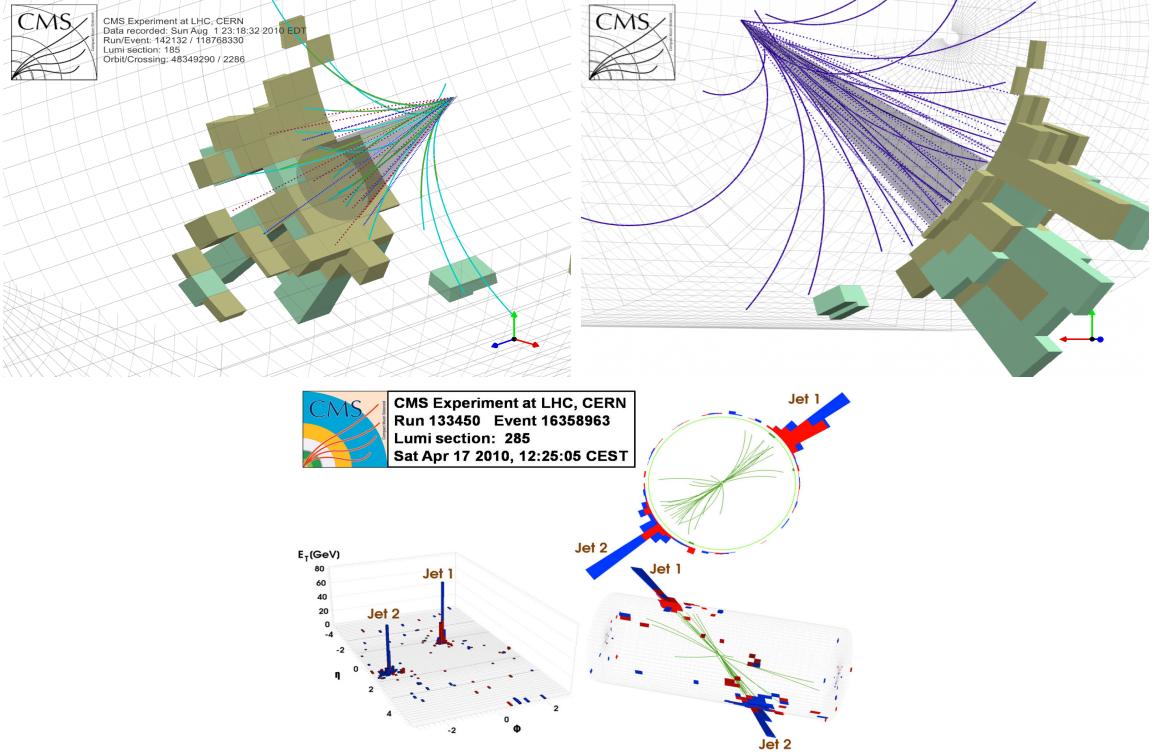


**Figure 4.3:** Jet reconstruction performed by the anti- $k_t$  algorithm. Top: Two different views of a CMS recorded event are presented. Continuous lines correspond to tracks left by charged particles in the tracker while dotted lines are the imaginary paths followed by neutral particles. The green cubes represent the ECAL cells while the blue ones represent the HCAL cells; in both cases, the height of the cube represent the amount of energy deposited in the cells [101]. Bottom: Reconstruction of a recorded event with two jets [102].

892 a new object whose momentum is the vectorial sum of the combined particles. If the  
 893 smallest distance is a  $d_{iB}$  the clustering process ends, the object  $i$  (which at this stage  
 894 should be a combination of several PF particles) is declared as a *Particle-flow-jet* (PF  
 895 jet) and all the associated PF particles are removed from the detector. The clustering  
 896 process is repeated until no PF particles remain.  
 897 Even though jets can be reconstructed efficiently, there are some effects that are not in-  
 898 cluded in the reconstruction and that lead to discrepancies between the reconstructed  
 899 results and the predicted results; in order to overcome these discrepancies, a factor-  
 900 ized model has been designed in the form of jet energy corrections (JEC) [103, 104]

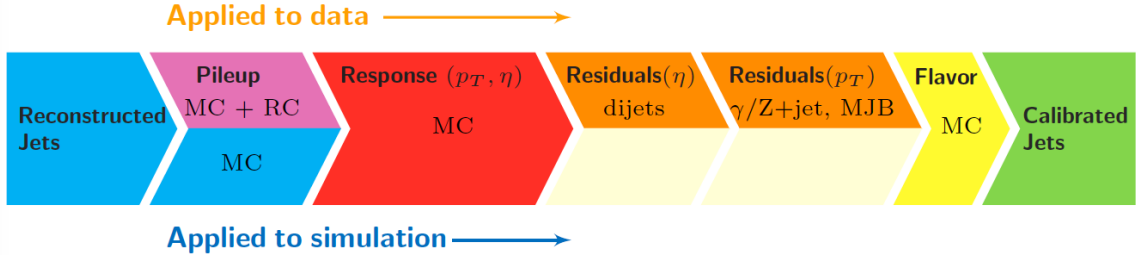


**Figure 4.4:** Jet energy correction diagram. Correction levels are applied sequentially in the indicated fixed order [104].

- 901 applied sequentially as shown in the diagram of Figure 4.4.
- 902 At each level, the jet four-momentum is multiplied by a scaling factor based on jet
- 903 properties, i.e.,  $\eta$ , flavor, etc.
- 904 • Level 1 correction removes the energy coming from pile-up. The scale factor is
- 905 determined using a MC sample of QCD dijet (2 jets) events with and without
- 906 pileup overlay; it is parametrized in terms of the offset energy density  $\rho$ , jet
- 907 area  $A$ , jet  $\eta$  and jet  $p_T$ . Different corrections are applied to data and MC due
- 908 to the detector simulation.
- 909 • MC-truth correction accounts for differences between the reconstructed jet en-
- 910 ergy and the MC particle-level energy. The correction is determined on a QCD
- 911 dijet MC sample and is parametrized in terms of the jet  $p_T$  and  $\eta$ .
- 912 • Residuals correct remaining small differences within jet response in data and
- 913 MC. The Residuals  $\eta$ -dependent correction compares jets of similar  $p_T$  in the
- 914 barrel reference region. The Residuals  $p_T$ -dependent correct the jet absolute
- 915 scale (JES vs  $p_T$ ).
- 916 • Jet-flavor corrections are derived in the same way as MC-truth corrections but
- 917 using QCD pure flavor samples.

918 ***b*-tagging of jets.**

919 A particular feature of the hadrons containing bottom quarks (*b*-hadrons) is that  
 920 their lifetime is long enough to travel some distance before decaying, but it is not as  
 921 long as those of light quark hadrons; therefore, when looking at the hadrons produced  
 922 in  $pp$  collisions, *b*-hadrons decay typically inside the tracker rather than reaching the  
 923 calorimeters as some light-hadrons do. As a result, a *b*-hadron decay gives rise to a  
 924 displaced vertex (secondary vertex) with respect to the primary vertex as shown in  
 925 Figure 4.5; the SV displacement is in the order of a few millimeters. A jet resulting  
 926 from the decay of a *b*-hadron is called *b* jet; other jets are called light jets.

927

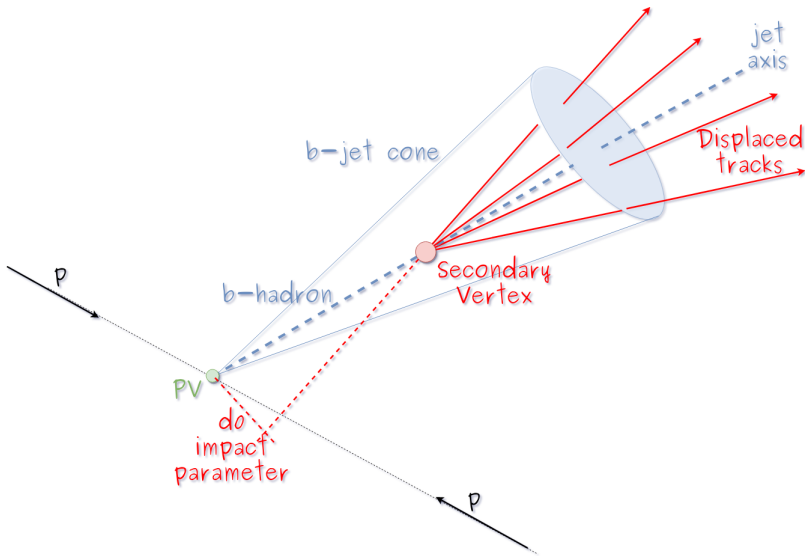


**Figure 4.5:** Secondary vertex in a *b*-hadron decay.

928 Several methods to identify *b*-jets (*b*-tagging) have been developed; the method used  
 929 in this thesis is known as *Combined Secondary Vertex* algorithm in its second version  
 930 (CSVv2) [105]. By using information of the impact parameter, the reconstructed  
 931 secondary vertices, and the jet kinematics as input in a multivariate analysis that  
 932 combines the discrimination power of each variable in one global discriminator vari-

able, three working points (references): loose, medium and tight, are defined which quantify the probabilities of mistag jets from light quarks as jets from  $b$  quarks; 10, 1 and 0.1 % respectively. Although the mistagging probability decreases with the working point strength, the efficiency to correctly tag  $b$ -jets also decreases as 83, 69 and 49 % for the respective working point; therefore, a balance needs to be achieved according to the specific requirements of the analysis.

#### 4.4.1.1 Missing transverse energy.

The fact that proton bunches carry momentum along the  $z$ -axis implies that for each event it is expected that the momentum in the transverse plane is balanced. Imbalances are quantified by the missing transverse energy (MET) and are attributed to several sources including particles escaping undetected through the beam pipe, neutrinos produced in weak interactions processes which do not interact with the detector and thus escaping without leaving a sign, or even undiscovered particles predicted by models beyond the SM.

947

948 The PF algorithm assigns the negative sum of the momenta of all reconstructed PF  
 949 particles to the *particle-flow MET* according to

$$\vec{E}_T = - \sum_i \vec{p}_{T,i} \quad (4.2)$$

950 JEC are propagated to the calculation of the  $\vec{E}_T$  as described in the Reference [106].

951

## 952 4.4.2 Event reconstruction examples

953 Figures 4.6-4.8 show the results of the reconstruction performed on 3 recorded events.

954 Descriptions are taken directly from the source.

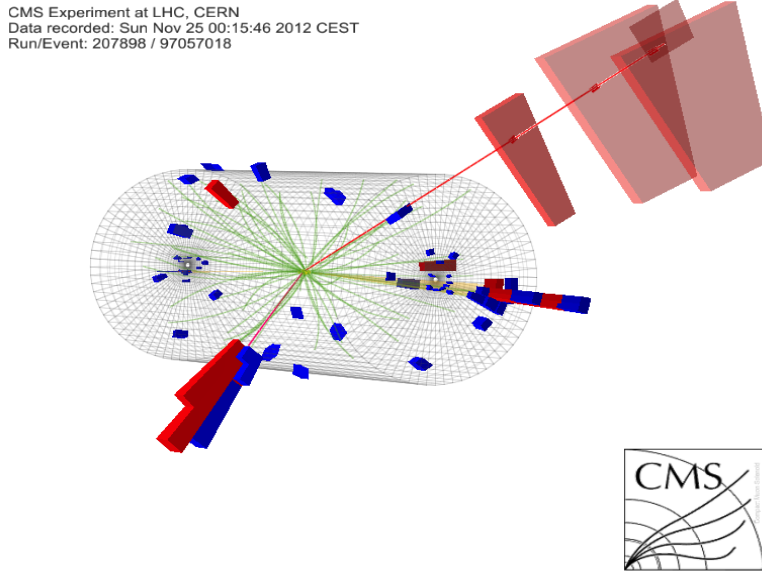


**Figure 4.6:** HIG-13-004 Event 1 reconstruction results; “HIG-13-004 Event 1: Event recorded with the CMS detector in 2012 at a proton-proton center-of-mass energy of 8 TeV. The event shows characteristics expected from the decay of the SM Higgs boson to a pair of  $\tau$  leptons. Such an event is characterized by the production of two forward-going jets, seen here in opposite endcaps. One of the  $\tau$  decays to a muon (red lines on the right) and neutrinos, while the other  $\tau$  decays into a charged hadron and a neutrino.” [107].

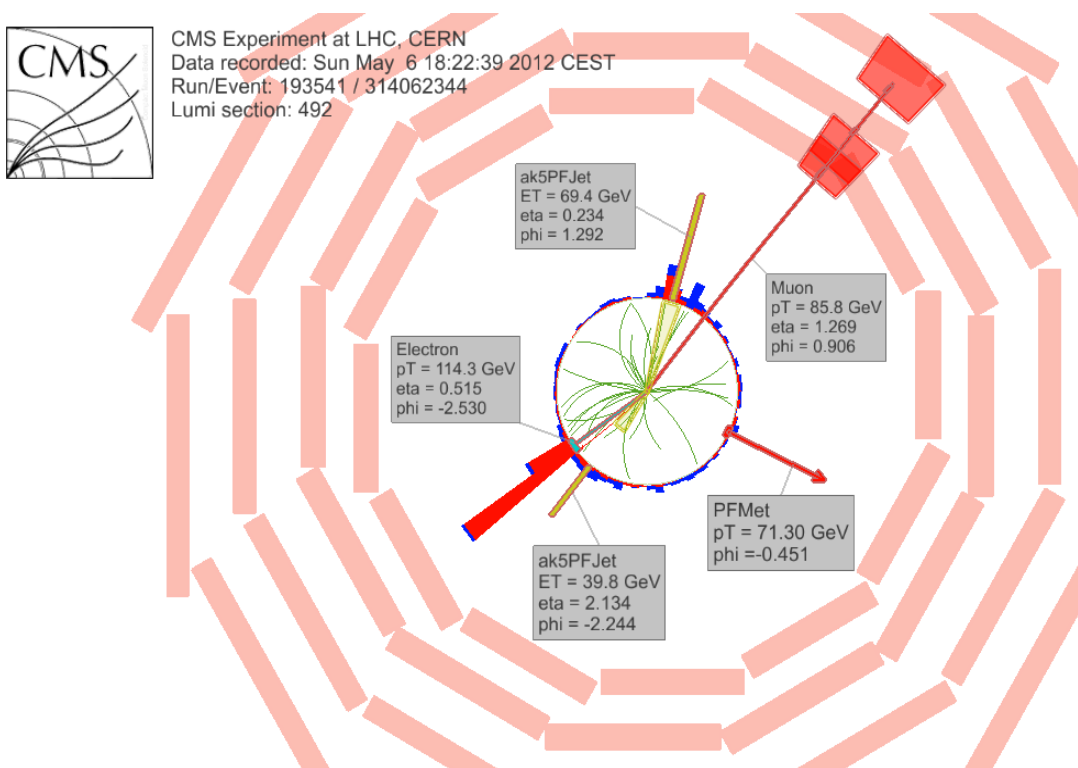


**Figure 4.7:**  $e\mu$  event reconstruction results; “An  $e\mu$  event candidate selected in 8 TeV data, as seen from the direction of the proton beams. The kinematics of the main objects used in the event selection are highlighted: two isolated leptons and two particle-flow jets. The reconstructed missing transverse energy is also displayed for reference” [108].

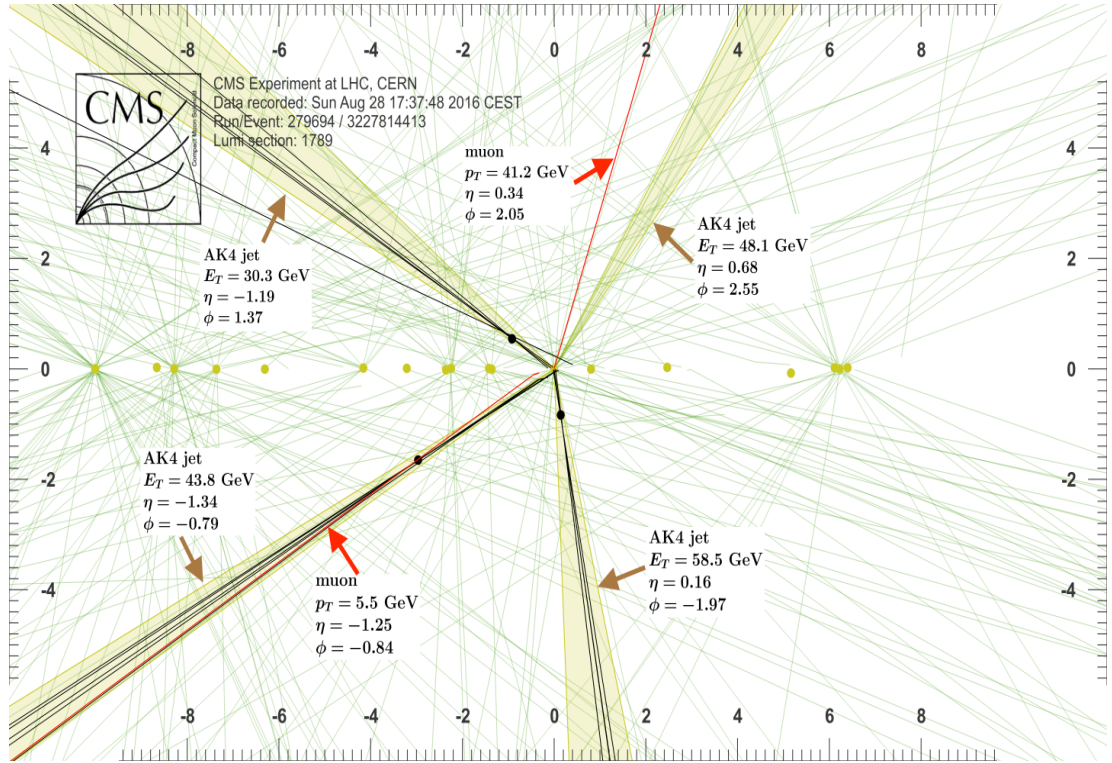


**Figure 4.8:** Recorded event reconstruction results;“Recorded event ( $\rho$ - $z$  projection) with three jets with  $p_T > 30$  GeV with one displaced muon track in 2016 data collected at 13 TeV. Each of the three jets has a displaced reconstructed vertex. The jet with  $p_T(j) = 43.8$  GeV,  $\eta(j) = -1.34$ ,  $\phi(j) = -0.79$  contains muon with  $p_T(\mu) = 5.5$  GeV,  $\eta(\mu) = -1.25$ ,  $\phi(\mu) = -0.84$ . Event contains reconstructed isolated muon with  $p_T(\mu) = 41.2$  GeV,  $\eta(\mu) = 0.34$ ,  $\phi(\mu) = 2.05$  and MET with  $p_T = 72.5$  GeV,  $\phi = -0.32$ . Jet candidates for a  $b$ -jet from top quark leptonic and hadronic decays are tagged by CSVv2T algorithm. One of the other two jets is tagged by CharmT algorithm. Tracks with  $p_T > 0.5$  GeV are shown. The number of reconstructed primary vertices is 18. Reconstructed  $m_T(W)$  is 101.8 GeV. Beam spot position correction is applied. Reconstructed primary vertices are shown in yellow color, while reconstructed displaced vertices and associated tracks are presented in black color. Dimensions are given in cm” [109].

955 

# References

- 956 [1] J. Schwinger. "Quantum Electrodynamics. I. A Covariant Formulation". Phys-  
 957       ical Review. 74 (10): 1439-61, (1948).
- 958 [2] R. P. Feynman. "Space-Time Approach to Quantum Electrodynamics". Physical  
 959       Review. 76 (6): 769-89, (1949).
- 960 [3] S. Tomonaga. "On a Relativistically Invariant Formulation of the Quantum  
 961       Theory of Wave Fields". Progress of Theoretical Physics. 1 (2): 27-42, (1946).
- 962 [4] D.J. Griffiths, "Introduction to electrodynamics". 4th ed. Pearson, (2013).
- 963 [5] F. Mandl, G. Shaw. "Quantum field theory." Chichester: Wiley (2009).
- 964 [6] F. Halzen, and A.D. Martin, "Quarks and leptons: An introductory course in  
 965       modern particle physics". New York: Wiley, (1984) .
- 966 [7] File: Standard\_Model\_of\_Elementary\_Particle\_dark.svg. (2017, June 12)  
 967       Wikimedia Commons, the free media repository. Retrieved November  
 968       27, 2017 from <https://www.collegiate-advanced-electricity.com/single-post/2017/04/10/The-Standard-Model-of-Particle-Physics>.
- 970 [8] E. Noether, "Invariante Variationsprobleme", Nachrichten von der Gesellschaft  
 971       der Wissenschaften zu Göttingen, mathematisch-physikalische Klasse, vol. 1918,  
 972       pp. 235-257, (1918).

- 973 [9] C. Patrignani et al. (Particle Data Group), Chin. Phys. C, 40, 100001 (2016)  
974 and 2017 update.
- 975 [10] M. Goldhaber, L. Grodzins, A.W. Sunyar “Helicity of Neutrinos”, Phys. Rev.  
976 109, 1015 (1958).
- 977 [11] Palanque-Delabrouille N et al. “Neutrino masses and cosmology with Lyman-  
978 alpha forest power spectrum”, JCAP 11 011 (2015).
- 979 [12] M. Gell-Mann. “A Schematic Model of Baryons and Mesons”. Physics Letters.  
980 8 (3): 214-215 (1964).
- 981 [13] G. Zweig. “An SU(3) Model for Strong Interaction Symmetry and its Breaking”  
982 (PDF). CERN Report No.8182/TH.401 (1964).
- 983 [14] G. Zweig. “An SU(3) Model for Strong Interaction Symmetry and its Breaking:  
984 II” (PDF). CERN Report No.8419/TH.412(1964).
- 985 [15] M. Gell-Mann. “The Interpretation of the New Particles as Displaced Charged  
986 Multiplets”. Il Nuovo Cimento 4: 848. (1956).
- 987 [16] T. Nakano, K, Nishijima. “Charge Independence for V-particles”. Progress of  
988 Theoretical Physics 10 (5): 581-582. (1953).
- 989 [17] N. Cabibbo, “Unitary symmetry and leptonic decays” Physical Review Letters,  
990 vol. 10, no. 12, p. 531, (1963).
- 991 [18] M.Kobayashi, T.Maskawa, “CP-violation in the renormalizable theory of weak  
992 interaction,” Progress of Theoretical Physics, vol. 49, no. 2, pp. 652-657, (1973).
- 993 [19] File: Weak Decay (flipped).svg. (2017, June 12). Wikimedia Com-  
994 mons, the free media repository. Retrieved November 27, 2017 from

- 995 https://commons.wikimedia.org/w/index.php?title=File:Weak\_Decay\_(flipped)  
996 .svg&oldid=247498592.
- 997 [20] Georgia Tech University. Coupling Constants for the Fundamental  
998 Forces(2005). Retrieved January 10, 2018, from http://hyperphysics.phy-  
999 astr.gsu.edu/hbase/Forces/couple.html#c2
- 1000 [21] M. Strassler. (May 31, 2013).The Strengths of the Known Forces. Retrieved Jan-  
1001 uary 10, 2018, from https://profmattstrassler.com/articles-and-posts/particle-  
1002 physics-basics/the-known-forces-of-nature/the-strength-of-the-known-forces/
- 1003 [22] S.L. Glashow. “Partial symmetries of weak interactions”, Nucl. Phys. 22 579-  
1004 588, (1961).
- 1005 [23] A. Salam, J.C. Ward. “Electromagnetic and weak interactions”, Physics Letters  
1006 13 168-171, (1964).
- 1007 [24] S. Weinberg, “A model of leptons”, Physical Review Letters, vol. 19, no. 21, p.  
1008 1264, (1967).
- 1009 [25] M. Peskin, D. Schroeder, “An introduction to quantum field theory”. Perseus  
1010 Books Publishing L.L.C., (1995).
- 1011 [26] A. Pich. “The Standard Model of Electroweak Interactions”  
1012 https://arxiv.org/abs/1201.0537
- 1013 [27] F.Bellaiche. (2012, 2 September). “What’s this Higgs boson anyway?”. Retrieved  
1014 from: https://www.quantum-bits.org/?p=233
- 1015 [28] M. Endres et al. Nature 487, 454-458 (2012) doi:10.1038/nature11255

- 1016 [29] F. Englert, R. Brout. “Broken Symmetry and the Mass of Gauge  
 1017 Vector Mesons”. Physical Review Letters. 13 (9): 321-23.(1964)  
 1018 doi:10.1103/PhysRevLett.13.321
- 1019 [30] P.Higgs. “Broken Symmetries and the Masses of Gauge Bosons”. Physical Re-  
 1020 view Letters. 13 (16): 508-509,(1964). doi:10.1103/PhysRevLett.13.508.
- 1021 [31] G.Guralnik, C.R. Hagen and T.W.B. Kibble. “Global Conservation Laws  
 1022 and Massless Particles”. Physical Review Letters. 13 (20): 585-587, (1964).  
 1023 doi:10.1103/PhysRevLett.13.585.
- 1024 [32] CMS collaboration. “Observation of a new boson at a mass of 125 GeV with  
 1025 the CMS experiment at the LHC”. Physics Letters B. 716 (1): 30-61 (2012).  
 1026 arXiv:1207.7235. doi:10.1016/j.physletb.2012.08.021
- 1027 [33] ATLAS collaboration. “Observation of a New Particle in the Search for the Stan-  
 1028 dard Model Higgs Boson with the ATLAS Detector at the LHC”. Physics Letters  
 1029 B. 716 (1): 1-29 (2012). arXiv:1207.7214. doi:10.1016/j.physletb.2012.08.020.
- 1030 [34] ATLAS collaboration; CMS collaboration (26 March 2015). “Combined Mea-  
 1031 surement of the Higgs Boson Mass in pp Collisions at  $\sqrt{s}=7$  and 8 TeV with  
 1032 the ATLAS and CMS Experiments”. Physical Review Letters. 114 (19): 191803.  
 1033 arXiv:1503.07589. doi:10.1103/PhysRevLett.114.191803.
- 1034 [35] LHC InternationalMasterclasses“When protons collide”. Retrieved from [http://atlas.physicsmasterclasses.org/en/zpath\\_protoncollisions.htm](http://atlas.physicsmasterclasses.org/en/zpath_protoncollisions.htm)  
 1035
- 1036 [36] CMS Collaboration, “SM Higgs Branching Ratios and Total Decay Widths (up-  
 1037 date in CERN Report4 2016)”. <https://twiki.cern.ch/twiki/bin/view/LHCPhysics/CERNYellowReportPageBR> , last accessed on 17.12.2017.  
 1038

- 1039 [37] R.Grant V. “Determination of Higgs branching ratios in  $H \rightarrow W^+W^- \rightarrow l\nu jj$   
 1040 and  $H \rightarrow ZZ \rightarrow l^+l^-jj$  channels”. Physics Department, University of Tennessee  
 1041 (Dated: October 31, 2012). Retrieved from <http://aesop.phys.utk.edu/ph611/2012/projects/Riley.pdf>
- 1043 [38] LHC Higgs Cross Section Working Group, Denner, A., Heinemeyer, S. et al.  
 1044 “Standard model Higgs-boson branching ratios with uncertainties”. Eur. Phys.  
 1045 J. C (2011) 71: 1753. <https://doi.org/10.1140/epjc/s10052-011-1753-8>
- 1046 [39] F. Maltoni, K. Paul, T. Stelzer, and S. Willenbrock, “Associated production  
 1047 of Higgs and single top at hadron colliders”, Phys.Rev. D64 (2001) 094023,  
 1048 [hep-ph/0106293].
- 1049 [40] S. Biswas, E. Gabrielli, F. Margaroli, and B. Mele, “Direct constraints on the  
 1050 top-Higgs coupling from the 8 TeV LHC data,” Journal of High Energy Physics,  
 1051 vol. 07, p. 073, (2013).
- 1052 [41] M. Farina, C. Grojean, F. Maltoni, E. Salvioni, and A. Thamm, “Lifting de-  
 1053 generacies in Higgs couplings using single top production in association with a  
 1054 Higgs boson,” Journal of High Energy Physics, vol. 05, p. 022, (2013).
- 1055 [42] T.M. Tait and C.-P. Yuan, “Single top quark production as a window to physics  
 1056 beyond the standard model”, Phys. Rev. D 63 (2000) 014018 [hep-ph/0007298].
- 1057 [43] F. Demartin, F. Maltoni, K. Mawatari, and M. Zaro, “Higgs production in  
 1058 association with a single top quark at the LHC,” European Physical Journal C,  
 1059 vol. 75, p. 267, (2015).

- 1060 [44] CMS Collaboration, “Modelling of the single top-quark production in associa-  
 1061 tion with the Higgs boson at 13 TeV.” [https://twiki.cern.ch/twiki/bin/](https://twiki.cern.ch/twiki/bin/viewauth/CMS/SingleTopHiggsGeneration13TeV)  
 1062 [viewauth/CMS/SingleTopHiggsGeneration13TeV](#), last accessed on 16.01.2018.
- 1063 [45] CMS Collaboration, “SM Higgs production cross sections at  $\sqrt{s} =$   
 1064 13 TeV.” [https://twiki.cern.ch/twiki/bin/](https://twiki.cern.ch/twiki/bin/view/LHCPhysics/CERNYellowReportPageAt13TeV)  
 1065 [view/LHCPhysics/CERNYellowReportPageAt13TeV](#), last accessed on 16.01.2018.
- 1066 [46] S. Dawson, The effective W approximation, Nucl. Phys. B 249 (1985) 42.
- 1067 [47] S. Biswas, E. Gabrielli and B. Mele, JHEP 1301 (2013) 088 [[arXiv:1211.0499](https://arxiv.org/abs/1211.0499)  
 1068 [hep-ph]].
- 1069 [48] F. Demartin, B. Maier, F. Maltoni, K. Mawatari, and M. Zaro, “tWH associated  
 1070 production at the LHC”, European Physical Journal C, vol. 77, p. 34, (2017).  
 1071 [arXiv:1607.05862](https://arxiv.org/abs/1607.05862)
- 1072 [49] LHC Higgs Cross Section Working Group, “Handbook of LHC Higgs Cross  
 1073 Sections: 4.Deciphering the Nature of the Higgs Sector”, [arXiv:1610.07922](https://arxiv.org/abs/1610.07922).
- 1074 [50] J. Ellis, D. S. Hwang, K. Sakurai, and M. Takeuchi.“Disentangling Higgs-Top  
 1075 Couplings in Associated Production”, JHEP 1404 (2014) 004, [[arXiv:1312.5736](https://arxiv.org/abs/1312.5736)].
- 1076 [51] CMS Collaboration, V. Khachatryan et al., “Precise determination of the mass  
 1077 of the Higgs boson and tests of compatibility of its couplings with the standard  
 1078 model predictions using proton collisions at 7 and 8 TeV,” [arXiv:1412.8662](https://arxiv.org/abs/1412.8662).
- 1079 [52] ATLAS Collaboration, G. Aad et al., “Updated coupling measurements of the  
 1080 Higgs boson with the ATLAS detector using up to  $25 \text{ fb}^{-1}$  of proton-proton  
 1081 collision data”, ATLAS-CONF-2014-009.

- 1082 [53] ATLAS and CMS Collaborations, “Measurements of the Higgs boson produc-  
1083 tion and decay rates and constraints on its couplings from a combined ATLAS  
1084 and CMS analysis of the LHC pp collision data at  $\sqrt{s} = 7$  and 8 TeV,” (2016).  
1085 CERN-EP-2016-100, ATLAS-HIGG-2015-07, CMS-HIG-15-002.
- 1086 [54] File:Cern-accelerator-complex.svg. Wikimedia Commons,  
1087 the free media repository. Retrieved January, 2018 from  
1088 <https://commons.wikimedia.org/wiki/File:Cern-accelerator-complex.svg>
- 1089 [55] J.L. Caron , “Layout of the LEP tunnel including future LHC infrastructures.”,  
1090 (Nov, 1993). A C Collection. Legacy of AC. Pictures from 1992 to 2002. Re-  
1091 trieved from <https://cds.cern.ch/record/841542>
- 1092 [56] M. Vretenar, “The radio-frequency quadrupole”. CERN Yellow Report CERN-  
1093 2013-001, pp.207-223 DOI:10.5170/CERN-2013-001.207. arXiv:1303.6762
- 1094 [57] L.Evans. P. Bryant (editors). “LHC Machine”. JINST 3 S08001 (2008).
- 1095 [58] CERN Photographic Service.“Radio-frequency quadrupole, RFQ-1”, March  
1096 1983, CERN-AC-8303511. Retrieved from <https://cds.cern.ch/record/615852>.
- 1097 [59] CERN Photographic Service “Animation of CERN’s accelerator net-  
1098 work”, 14 October 2013. DOI: 10.17181/cds.1610170 Retrieved from  
1099 <https://videos.cern.ch/record/1610170>
- 1100 [60] C.Sutton. “Particle accelerator”.Encyclopedia Britannica. July 17, 2013. Re-  
1101 trieved from <https://www.britannica.com/technology/particle-accelerator>.
- 1102 [61] L.Guiraud. “Installation of LHC cavity in vacuum tank.”. July 27 2000. CERN-  
1103 AC-0007016. Retrieved from <https://cds.cern.ch/record/41567>.

- 1104 [62] J.L. Caron, “Magnetic field induced by the LHC dipole’s superconducting coils”.  
1105 March 1998. AC Collection. Legacy of AC. Pictures from 1992 to 2002. LHC-  
1106 PHO-1998-325. Retrieved from <https://cds.cern.ch/record/841511>
- 1107 [63] AC Team. “Diagram of an LHC dipole magnet”. June 1999. CERN-DI-9906025  
1108 retrieved from <https://cds.cern.ch/record/40524>.
- 1109 [64] CMS Collaboration “Public CMS Luminosity Information”.  
1110 <https://twiki.cern.ch/twiki/bin/view/CMSPublic/LumiPublicResults#2016>  
1111 \_proton\_proton\_13\_TeV\_collis, last accessed 24.01.2018
- 1112 [65] J.L. Caron. “LHC Layout” AC Collection. Legacy of AC. Pictures  
1113 from 1992 to 2002. September 1997, LHC-PHO-1997-060. Retrieved from  
1114 <https://cds.cern.ch/record/841573>.
- 1115 [66] J.A. Coarasa. “The CMS Online Cluster: Setup, Operation and Maintenance  
1116 of an Evolving Cluster”. ISGC 2012, 26 February - 2 March 2012, Academia  
1117 Sinica, Taipei, Taiwan.
- 1118 [67] CMS Collaboration. “The CMS experiment at the CERN LHC” JINST 3 S08004  
1119 (2008).
- 1120 [68] CMS Collaboration. “CMS detector drawings 2012” CMS-PHO-GEN-2012-002.  
1121 Retrieved from <http://cds.cern.ch/record/1433717>.
- 1122 [69] R. Breedon. “View through the CMS detector during the cooldown of the  
1123 solenoid on February 2006. CMS Collection”, February 2006, CMS-PHO-  
1124 OREACH-2005-004, Retrieved from <https://cds.cern.ch/record/930094>.
- 1125 [70] A. Dominguez et. al. “CMS Technical Design Report for the Pixel Detector  
1126 Upgrade”, CERN-LHCC-2012-016. CMS-TDR-11.

- 1127 [71] CMS Collaboration. “Description and performance of track and primary-vertex  
1128 reconstruction with the CMS tracker,” Journal of Instrumentation, vol. 9, no.  
1129 10, p. P10009,(2014).
- 1130 [72] CMS Collaboration and M. Brice. “Images of the CMS Tracker Inner  
1131 Barrel”, November 2008, CMS-PHO-TRACKER-2008-002. Retrieved from  
1132 <https://cds.cern.ch/record/1431467>.
- 1133 [73] M. Weber. “The CMS tracker”. 6th international conference on hyperons, charm  
1134 and beauty hadrons Chicago, June 28-July 3 2004.
- 1135 [74] CMS Collaboration. “Projected Performance of an Upgraded CMS Detector at  
1136 the LHC and HL-LHC: Contribution to the Snowmass Process”. Jul 26, 2013.  
1137 arXiv:1307.7135
- 1138 [75] L. Veillet. “End assembly of HB with EB rails and rotation in-  
1139 side SX ”,January 2002. CMS-PHO-HCAL-2002-002. Retrieved from  
1140 <https://cds.cern.ch/record/42594>.
- 1141 [76] J. Puerta-Pelayo.“First DT+RPC chambers installation round in the  
1142 UX5 cavern.”. January 2007, CMS-PHO-OREACH-2007-001. Retrieved from  
1143 <https://cds.cern.ch/record/1019185>
- 1144 [77] X. Cid Vidal and R. Cid Manzano. “CMS Global Muon Trigger” web  
1145 site: Taking a closer look at LHC. Retrieved from [https://www.lhc-closer.es/taking\\_a\\_closer\\_look\\_at\\_lhc/0.lhc\\_trigger](https://www.lhc-closer.es/taking_a_closer_look_at_lhc/0.lhc_trigger)
- 1147 [78] WLCG Project Office, “Documents & Reference - Tiers - Structure,” (2014).  
1148 <http://wlcg.web.cern.ch/documents-reference> , last accessed on 30.01.2018.

- 1149 [79] CMS Collaboration. “CMSSW Application Framework”,  
 1150 <https://twiki.cern.ch/twiki/bin/view/CMSPublic/WorkBookCMSSWFramework>,  
 1151 last accesses 06.02.2018
- 1152 [80] A. Buckleya, J. Butterworthb, S. Giesekec, et. al. “General-purpose event gen-  
 1153 erators for LHC physics”. arXiv:1101.2599v1 [hep-ph] 13 Jan 2011
- 1154 [81] A. Quadt. “Top Quark Physics at Hadron Colliders”. Advances in the Physics  
 1155 of Particles and Nuclei. Springer-Verlag Berlin Heidelberg. DOI: 10.1007/978-  
 1156 3-540-71060-8 (2007)
- 1157 [82] DurhamHep Data Project, “The Durham HepData Project - PDF Plotter.”  
 1158 <http://hepdata.cedar.ac.uk/pdf/pdf3.html> , last accessed on 02.02.2018.
- 1159 [83] F. Maltoni, G. Ridolfi, and M. Ubiali, “b-initiated processes at the LHC: a  
 1160 reappraisal,” Journal of High Energy Physics, vol. 07, p. 022, (2012).
- 1161 [84] B. Andersson, G. Gustafson, G.Ingelman and T. Sjostrand, “Parton fragmen-  
 1162 tation and string dynamics”, Physics Reports, Vol. 97, No. 2-3, pp. 31-145,  
 1163 1983.
- 1164 [85] CMS Collaboration, “Event generator tunes obtained from underlying event  
 1165 and multiparton scattering measurements;” European Physical Journal C, vol.  
 1166 76, no. 3, p. 155, (2016).
- 1167 [86] J. Alwall et. al., “The automated computation of tree-level and next-to-leading  
 1168 order differential cross sections, and their matching to parton shower simula-  
 1169 tions,” Journal of High Energy Physics, vol. 07, p. 079, (2014).

- 1170 [87] S. Frixione, P. Nason, and C. Oleari, “Matching NLO QCD computations with  
1171 Parton Shower simulations: the POWHEG method,” Journal of High Energy  
1172 Physics, vol. 11, p. 070, (2007).
- 1173 [88] S. Agostinelli et al., “GEANT4: A Simulation toolkit,” Nuclear Instruments  
1174 and Methods in Physics, vol. A506, pp. 250–303, (2003).
- 1175 [89] J.Allison et.al.,“Recent developments in Geant4”, Nuclear Instruments and  
1176 Methods in Physics Research A 835 (2016) 186-225.
- 1177 [90] CMS Collaboration “Full Simulation Offline Guide”, <https://twiki.cern.ch/twiki/bin/view/CMSPublic/SWGuideSimulation>, last accessed 04.02.2018
- 1179 [91] A. Giammanco. “The Fast Simulation of the CMS Experiment” J. Phys.: Conf.  
1180 Ser. 513 022012 (2014)
- 1181 [92] A.M. Sirunyan et. al. “Particle-flow reconstruction and global event description  
1182 with the CMS detector”, JINST 12 P10003 (2017) <https://doi.org/10.1088/1748-0221/12/10/P10003>.
- 1184 [93] The CMS Collaboration. “ Description and performance of track and pri-  
1185 mary vertex reconstruction with the CMS tracker”. JINST 9 P10009 (2014).  
1186 doi:10.1088/1748-0221/9/10/P10009
- 1187 [94] J. Incandela. “Status of the CMS SM Higgs Search” July 4, 2012. Pdf slides.  
1188 Retrieved from [https://indico.cern.ch/event/197461/contributions/1478917/attachments/290954/406673/CMS\\_4July2012\\_Final.pdf](https://indico.cern.ch/event/197461/contributions/1478917/attachments/290954/406673/CMS_4July2012_Final.pdf)
- 1190 [95] P. Billoir and S. Qian, “Simultaneous pattern recognition and track fitting by  
1191 the Kalman filtering method”, Nucl. Instrum. Meth. A 294 219. (1990).

- 1192 [96] W. Adam, R. Fruhwirth, A. Strandlie and T. Todorov, “Reconstruction of  
 1193 electrons with the Gaussian sum filter in the CMS tracker at LHC”, eConf  
 1194 C 0303241 (2003) TULT009 [physics/0306087].
- 1195 [97] K. Rose, “Deterministic Annealing for Clustering, Compression, Classification,  
 1196 Regression and related Optimisation Problems”, Proc. IEEE 86 (1998) 2210.
- 1197 [98] R. Fruhwirth, W. Waltenberger and P. Vanlaer, “ Adaptive Vertex Fitting”,  
 1198 CMS Note 2007-008 (2007).
- 1199 [99] CMS collaboration, “Performance of CMS muon reconstruction in pp collision  
 1200 events at  $\sqrt{s} = 7$  TeV ”, JINST 7 P10002 2012, [arXiv:1206.4071].
- 1201 [100] M. Cacciari, G. P. Salam, and G. Soyez, “The anti- $k_t$  jet clustering algorithm,”  
 1202 Journal of High Energy Physics, vol. 04, p. 063, (2008).
- 1203 [101] B. Dorney. “Anatomy of a Jet in CMS”. Quantum Diaries. June  
 1204 1st, 2011. Retrieved from <https://www.quantumdiaries.org/2011/06/01/anatomy-of-a-jet-in-cms/>
- 1206 [102] The CMS Collaboration.“Event Displays from the high-energy collisions at 7  
 1207 TeV”, May 2010, CMS-PHO-EVENTS-2010-007, Retrieved from <https://cds.cern.ch/record/1429614>.
- 1209 [103] The CMS collaboration. “Determination of jet energy calibration and transverse  
 1210 momentum resolution in CMS”. JINST 6 P11002 (2011). <http://dx.doi.org/10.1088/1748-0221/6/11/P11002>
- 1212 [104] The CMS Collaboration, “Introduction to Jet Energy Corrections at  
 1213 CMS.”. <https://twiki.cern.ch/twiki/bin/view/CMS/IntroToJEC>, last ac-  
 1214 cessed 10.02.2018.

- 1215 [105] CMS Collaboration Collaboration. “Identification of b quark jets at the CMS  
 1216 Experiment in the LHC Run 2”. Tech. rep. CMS-PAS-BTV-15-001. Geneva:  
 1217 CERN, (2016). <https://cds.cern.ch/record/2138504>.
- 1218 [106] CMS Collaboration Collaboration. “Performance of missing energy reconstruc-  
 1219 tion in 13 TeV pp collision data using the CMS detector”. Tech. rep. CMS-PAS-  
 1220 JME16-004. Geneva: CERN, 2016. <https://cds.cern.ch/record/2205284>.
- 1221 [107] CMS Collaboration, “New CMS results at Moriond (Electroweak) 2013”,  
 1222 Retrieved from <http://cms.web.cern.ch/sites/cms.web.cern.ch/files/>  
 1223 [styles/large/public/field/image/HIG13004\\_Event01\\_0.png?itok=L AwZzPHR](#)
- 1224
- 1225 [108] CMS Collaboration, “New CMS results at Moriond (Electroweak) 2013”,  
 1226 Retrieved from <http://cms.web.cern.ch/sites/cms.web.cern.ch/>  
 1227 [files/styles/large/public/field/image/TOP12035\\_Event01.png?itok=uMdnSqzC](#)
- 1228
- 1229 [109] K. Skovpen. “Event displays highlighting the main properties of heavy flavour  
 1230 jets in the CMS Experiment”, Aug 2017, CMS-PHO-EVENTS-2017-006. Re-  
 1231 trievied from <https://cds.cern.ch/record/2280025>.
- 1232 [110] G. Cowan. “Topics in statistical data analysis for high-energy physics”.  
 1233 arXiv:1012.3589v1
- 1234 [111] A. Hoecker et al., “TMVA-Toolkit for multivariate data analysis”  
 1235 arXiv:physics/0703039v5 (2009)

- 1236 [112] L. Lista. “Statistical Methods for Data Analysis in Particle Physics”, 2nd  
 1237 ed. Springer International Publishing. (2017) <https://dx.doi.org/10.1007/978-3-319-62840-0>
- 1239 [113] I. Antcheva et al., “ROOT-A C++ framework for petabyte data storage, sta-  
 1240 tistical analysis and visualization ,” Computer Physics Communications, vol.  
 1241 182, no. 6, pp. 1384â€¢1385, (2011).
- 1242 [114] Y. Coadou. “Boosted decision trees”, ESIPAP, Archamps, 9 Febru-  
 1243 ary 2016. Lecture. Retrieved from [https://indico.cern.ch/event/472305/contributions/1982360/attachments/1224979/1792797/ESIPAP\\_MVA160208-BDT.pdf](https://indico.cern.ch/event/472305/contributions/1982360/attachments/1224979/1792797/ESIPAP_MVA160208-BDT.pdf)
- 1246 [115] J.H. Friedman. “Greedy function approximation: A gradient boosting ma-  
 1247 chine”. Ann. Statist. Volume 29, Number 5 (2001), 1189-1232. [https://projecteuclid.org/download/pdf\\_1/euclid-aos/1013203451](https://projecteuclid.org/download/pdf_1/euclid-aos/1013203451).
- 1249 [116] F. James, M. Roos, “MINUIT: Function minimization and error analysis”. Cern  
 1250 Computer Centre Program Library, Geneve Long Write-up No. D506, 1989
- 1251 [117] J. Neyman and E. S. Pearson, “On the problem of the most efficient tests  
 1252 of statistical hypotheses”. Philosophical Transactions of the Royal Society of  
 1253 London. Series A, Containing Papers of a Mathematical or Physical Character.  
 1254 Vol. 231 (1933), pp. 289-337
- 1255 [118] B. Hespel, F. Maltoni, and E. Vryonidou, “Higgs and Z boson associated pro-  
 1256 duction via gluon fusion in the SM and the 2HDM”, JHEP 06 (2015) 065,  
 1257 doi:10.1007/JHEP06(2015)065, arXiv:1503.01656.

- 1258 [119] ATLAS Collaboration, “Measurements of Higgs boson produc-  
 1259 tion and couplings in diboson final states with the ATLAS  
 1260 detector at the LHC”, Phys. Lett. B726 (2013) 88–119,  
 1261 doi:10.1016/j.physletb.2014.05.011,10.1016/j.physletb.2013.08.010,  
 1262 arXiv:1307.1427. [Erratum: Phys. Lett.B734,406(2014)].
- 1263 [120] CMS Collaboration, “Search for the associated production of a Higgs boson  
 1264 with a single top quark in proton-proton collisions at  $\sqrt{s} = 8$  TeV”, JHEP 06  
 1265 (2016) 177,doi:10.1007/JHEP06(2016)177, arXiv:1509.08159.
- 1266 [121] B. Stieger, C. Jorda Lope et al., “Search for Associated Production of a Single  
 1267 Top Quark and a Higgs Boson in Leptonic Channels”, CMS Analysis Note CMS  
 1268 AN-14-140, 2014.
- 1269 [122] M. Peruzzi, C. Mueller, B. Stieger et al., “Search for ttH in multilepton final  
 1270 states at  $\sqrt{s} = 13$  TeV”, CMS Analysis Note CMS AN-16-211, 2016.
- 1271 [123] CMS Collaboration, “Search for H to bbar in association with a single top quark  
 1272 as a test of Higgs boson couplings at  $\sqrt{s} = 13$  TeV”, CMS Physics Analysis  
 1273 Summary CMS-PAS-HIG-16-019, 2016.
- 1274 [124] CMS Collaboration, “Search for production of a Higgs boson and a single top  
 1275 quark in multilepton final states in proton collisions at  $\sqrt{s} = 13$  TeV”, CMS  
 1276 Physics Analysis Summary CMS-PAS-HIG-17-005, 2016.
- 1277 [125] B. WG, “BtagRecommendation80XReReco”, February, 2017. <https://twiki.cern.ch/twiki/bin/view/CMS/BtagRecommendation80XReReco>.

1279 [126] CMS Collaboration, “Identification of b quark jets at the CMS Experiment  
1280 in the LHC Run 2”, CMS Physics Analysis Summary CMS-PAS-BTV-15-001,  
1281 2016.

1282 [127] M. Peruzzi, F. Romeo, B. Stieger et al., “Search for ttH in multilepton final1  
1283 states at  $\sqrt{s} = 13$  TeV”, CMS Analysis Note CMS AN-17-029, 2017.

1284 [128] CMS Collaboration, “Baseline muon selections for Run-II.” <https://twiki.cern.ch/twiki/bin/view/CMSPublic/SWGuideMuonIdRun2>, last accessed on  
1285 24.02.2018.

1287 [129] G. Petrucciani and C. Botta, “Two step prompt muon identification”, January,  
1288 2015. <https://indico.cern.ch/event/368007/contribution/2/material/slides/0.pdf>.

1290 [130] H. Brun and C. Ochando, “Updated Results on MVA eID with 13 TeV samples”,  
1291 October, 2014. <https://indico.cern.ch/event/298249/contribution/3/material/slides/0.pdf>.

1293 [131] B. Maier, “SingleTopHiggProduction13TeV”, February, 2016.  
1294 <https://twiki.cern.ch/twiki/bin/viewauth/CMS/SingleTopHiggsGeneration13TeV>.